



# POWDERDAY: Dust Radiative Transfer for Galaxy Simulations

Desika Narayanan<sup>1,2,3</sup>, Matthew J. Turk<sup>4,5</sup>, Thomas Robitaille<sup>6</sup>, Ashley J. Kelly<sup>7</sup>, B. Connor McClellan<sup>8</sup>, Ray S. Sharma<sup>9</sup>, Prerak Garg<sup>1</sup>, Matthew Abruzzo<sup>10</sup>, Ena Choi<sup>11</sup>, Charlie Conroy<sup>12</sup>, Benjamin D. Johnson<sup>12</sup>, Benjamin Kimock<sup>1</sup>, Qi Li<sup>1</sup>, Christopher C. Lovell<sup>13</sup>, Sidney Lower<sup>1</sup>, George C. Privon<sup>1,14</sup>, Jonathan Roberts<sup>1</sup>, Snigdaa Sethuram<sup>9,15</sup>, Gregory F. Snyder<sup>16</sup>, Robert Thompson<sup>17</sup>, and John H. Wise<sup>15</sup>

<sup>1</sup> Department of Astronomy, University of Florida, 211 Bryant Space Science Center, Gainesville, FL 32611, USA; [desika.narayanan@ufl.edu](mailto:desika.narayanan@ufl.edu)

<sup>2</sup> University of Florida Informatics Institute, 432 Newell Drive, CISE Bldg E251, Gainesville, FL 32611, USA

<sup>3</sup> Cosmic Dawn Center at the Niels Bohr Institute, University of Copenhagen and DTU-Space, Technical University of Denmark, Denmark

<sup>4</sup> School of Information Sciences, University of Illinois, Urbana-Champaign, IL 61820, USA

<sup>5</sup> Department of Astronomy, University of Illinois, Urbana-Champaign, IL 61820, USA

<sup>6</sup> Aperio Software, Headingley Enterprise & Arts Centre, Bennett Road, Leeds LS6 3HN, UK

<sup>7</sup> Institute for Computational Cosmology, Department of Physics, Durham University, South Road, Durham, DH1 3LE, UK

<sup>8</sup> Department of Astronomy, University of Virginia, 530 McCormick Road, Charlottesville, VA 22904, USA

<sup>9</sup> Rutgers, the State University of New Jersey, 136 Frelinghuysen Road, Piscataway, NJ 08854, USA

<sup>10</sup> Department of Astronomy, Columbia University, New York, NY 10027, USA

<sup>11</sup> Quantum Universe Center, Korea Institute for Advanced Study, Hoegiro 85, Seoul 02455, Republic of Korea

<sup>12</sup> Center for Astrophysics, Harvard & Smithsonian, 60 Garden Street, Cambridge, MA 02138, USA

<sup>13</sup> Centre for Astrophysical Research, School of Physics, Astronomy and Mathematics, University of Hertfordshire, Hatfield, AL10 9AB, UK

<sup>14</sup> National Radio Astronomy Observatory, 520 Edgemont Road, Charlottesville, VA 22903, USA

<sup>15</sup> Center for Relativistic Astrophysics, School of Physics, Georgia Institute of Technology, 837 State Street, Atlanta, GA 30332, USA

<sup>16</sup> Space Telescope Science Institute, 3700 San Martin Drive, Baltimore, MD 21218, USA

<sup>17</sup> Portalium, 3410 Far West Boulevard, Austin, TX 78731, USA

Received 2020 June 18; revised 2020 October 5; accepted 2020 October 23; published 2021 January 13

## Abstract

We present POWDERDAY (available at <https://github.com/dnarayanan/powderday>), a flexible, fast, open-source dust radiative transfer package designed to interface with both idealized and cosmological galaxy formation simulations. POWDERDAY builds on FSPS stellar population synthesis models, and HYPERION dust radiative transfer, and employs YT to interface between different software packages. We include our stellar population synthesis modeling on the fly, allowing significant flexibility in the assumed stellar physics and nebular line emission. The dust content follows either simple observationally motivated prescriptions (i.e., constant dust-to-metals ratios, or dust-to-gas ratios that vary with metallicity), direct modeling from galaxy formation simulations that include dust physics, as well as a novel approach that includes the dust content via learning-based algorithms from the SIMBA cosmological galaxy formation simulation. Active galactic nuclei (AGNs) can additionally be included via a range of prescriptions. The output of these models are broadband (912 Å–1 mm) spectral energy distributions (SEDs), as well as filter-convolved monochromatic images. POWDERDAY is designed to eliminate last-mile efforts by researchers that employ different hydrodynamic galaxy formation models and seamlessly interfaces with GIZMO, AREPO, GASOLINE, CHANGA, and ENZO. We demonstrate the capabilities of the code via three applications: a model for the star formation rate–infrared luminosity relation in galaxies (including the impact of AGNs), the impact of circumstellar dust around AGB stars on the mid-infrared emission from galaxy SEDs, and the impact of galaxy inclination angle on dust attenuation laws.

*Unified Astronomy Thesaurus concepts:* Galaxy evolution (594); Galaxy luminosities (603); Astronomy software (1855); Open source software (1866); Radiative transfer simulations (1967)

## 1. Introduction

The turn of the century ushered in dramatic advances in our knowledge of cosmological galaxy evolution. The advent of medium and ultra-deep surveys across the electromagnetic spectrum has resulted in the discovery of tens of thousands of galaxies through the first billion years after the Big Bang (e.g., Shapley 2011; Madau & Dickinson 2014; Finkelstein 2016; Stark 2016). These include populations of star-forming and passive galaxies at  $z \sim 2$  identified via novel color selection techniques (Steidel et al. 1996; Daddi et al. 2004; van Dokkum et al. 2008), galaxies at redshifts as large as  $z \sim 10$  (Finkelstein et al. 2013, 2015; Oesch et al. 2015, 2018), and large samples of dusty starburst galaxies selected in the infrared and submillimeter (Blain et al. 2002; Casey et al. 2014; Lutz 2014; Hodge & da Cunha 2020). Similarly, targeted surveys of nearby galaxies have increased our understanding of both their resolved stellar

populations and their molecular and dusty interstellar medium (ISM) properties (e.g., Kennicutt et al. 2003, 2011; Dalcanton et al. 2012). These surveys near and far have placed strong constraints on the cosmic evolution of the star formation rate (SFR) density, stellar mass, and the ISM content in galaxies (Blanton & Moustakas 2009; Kennicutt & Evans 2012; Carilli & Walter 2013; Madau & Dickinson 2014).

At the same time, simulations of galaxy formation have become increasingly sophisticated and shown substantial progress in their ability to reproduce and interpret observations (see the recent reviews by Benson 2010; Somerville & Davé 2015; Naab & Ostriker 2017; Vogelsberger et al. 2020). These simulations suggest a variety of mechanisms for shaping the physical properties of galaxies at different mass scales, including black hole growth and feedback, radiative feedback, gas accretion from the intergalactic medium, and supernova-driven feedback among many others. Promisingly,

despite the diverse range of methods used, cosmological galaxy formation simulations have converged on a number of predicted physical properties, including their predicted stellar mass functions,  $\text{SFR}-M_*$  relations, dust mass functions, and global gas fractions (Davé et al. 2012, 2013, 2019; Vogelsberger et al. 2014; Schaye et al. 2015; Somerville et al. 2015; Hopkins et al. 2018; Li et al. 2019). Of course, in detail, the physical properties of modeled galaxies are strongly dependent on prescriptions for physical processes on small scales such as star formation, black hole growth (and their associated feedback), chemistry, the structure of the ISM, and so on. Seemingly small differences in any given prescription can have dramatic effects on the observed properties of galaxies (e.g., Hopkins et al. 2013).

In order to quantitatively compare numerical simulations of galaxy formation and observations, one either needs to convert integrated observational measures into physical quantities output by the simulations or map the physical properties generated in simulations to bona fide observables. The former method typically relies on some sort of theoretical or empirical underpinning relating observed quantities to physical properties, which can introduce some level of uncertainty. For example, uncertainties in galaxy star formation histories, stellar evolution tracks, obscuring dust geometries, and the initial mass function propagate to uncertainties in derived SFRs and stellar masses of observed galaxies (e.g., Maraston et al. 2006; Conroy et al. 2009; Michałowski et al. 2010; Dunlop 2011; Walcher et al. 2011; Conroy 2013; Leja et al. 2017, 2019; Zhang et al. 2017; Lower et al. 2020). Similarly, uncertainties in spectral energy distribution (SED) modeling, or the conversion between emission-line strengths, continuum strengths, and gas masses are present in any measurement of the ISM properties of galaxies (e.g., Feldmann et al. 2011; Narayanan et al. 2011b, 2012; Casey 2012; Bolatto et al. 2013; Scoville et al. 2014; Liang et al. 2018; Privon et al. 2018).

As reviewed by Steinacker et al. (2013), one alternative to this is to utilize dust radiative transfer simulations to directly calculate observables from the physical properties of galaxy formation models. To do this requires generating SEDs for luminous sources and modeling the transfer of this radiation through the ISM. The application of dust radiative transfer models to galaxy simulations has a rich history. Indeed, a handful of both proprietary and open-source codes exist in the literature, including SUNRISE (Jonsson 2006; Jonsson & Primack 2010; Jonsson et al. 2010), SKIRT (Baes et al. 2011), RADISHE (Chakrabarti & Whitney 2009), DARTRAY (Natale et al. 2014), DIRTY (Gordon et al. 2001; Misselt et al. 2001), GRASIL (Domínguez-Tenreiro et al. 2014), RADMC3D (Dullemond et al. 2012), and ART<sup>2</sup> (Li et al. 2020). HYPERION (Robitaille 2011) is a flexible and generic dust radiative transfer code that, while not written specifically for galaxy formation simulations, can be used for them. We will discuss this particular code in much more detail later in this paper.

Beyond serving as a tool for assessing how realistic modeled galaxies are (by comparing their modeled morphologies or broadband colors to observations; Narayanan et al. 2011a; Law et al. 2012; Schaye et al. 2015; Snyder et al. 2015a, 2015b, 2017; Torrey et al. 2015; Abruzzo et al. 2018; Blecha et al. 2018; Rodriguez-Gomez et al. 2019), computational galaxy formation studies that have employed dust radiative transfer models have typically been used for two purposes. The

first is to understand the physical properties and formation mechanisms of particular galaxy populations (e.g., Efstathiou et al. 2000; Granato et al. 2000, 2015; Baugh et al. 2005; Chakrabarti et al. 2007, 2008; Narayanan et al. 2009, 2010a, 2010b, 2015; Younger et al. 2009; Hayward et al. 2011, 2013; Snyder et al. 2011; Cen & Kimm 2014; Cowley et al. 2015; Blecha et al. 2018; Kulier et al. 2019; McAlpine et al. 2019), as well as galaxy model verification (e.g., Trayford et al. 2017; Camps et al. 2018; Baes et al. 2019, 2020; Cochrane et al. 2019).

A second powerful way to utilize dust radiative transfer models is to investigate the ability of an observational tool in deriving physical quantities. For example, recent studies have investigated quantitative morphology measures (Lotz et al. 2010a, 2010b; Snyder et al. 2015a, 2019; Abruzzo et al. 2018; Cochrane et al. 2019), SFR indicators (De Looze et al. 2014; Hayward et al. 2014), stellar masses (Torrey et al. 2015; Baes et al. 2019; Katsianis et al. 2020; Lower et al. 2020), active galactic nuclei (AGNs) diagnostics (Narayanan et al. 2010b; Snyder et al. 2013), bulge-disk decomposition (Scannapieco et al. 2010), the stellar initial mass function (e.g., Baugh et al. 2005; Narayanan & Davé 2012, 2013; Cowley et al. 2019), dust temperatures (Liang et al. 2018, 2019; Privon et al. 2018; Ma et al. 2019), and galaxy dust attenuation curves (Narayanan et al. 2018a, 2018b; Ma et al. 2019; Trayford et al. 2020). While the aforementioned works couple radiative transfer with galaxy formation simulations, some complementary works have coupled 3D dust radiative transfer models with models for galaxies approximated with simplified geometries in order to both derive physical properties of observed galaxies and assess the efficacy of the diagnostic tools themselves (e.g., Pierini et al. 2004; Tuffs et al. 2004; Gadotti et al. 2010; Pastrav et al. 2013; De Looze et al. 2014).

Despite the fact that dust radiative transfer codes have existed in the literature for more than a decade, their usage with galaxy formation simulations is only becoming common-place in the last few years. This is due, in part, to the fact that they can be computationally demanding to run, as well as contain significant “last-mile” efforts often needed to ensure correct data formats, units, and model parameters that can vary significantly with different hydrodynamic codes. There is a need, in our view, for a dust radiative transfer package with several attributes that can overcome this. First, such a code would optimally be highly flexible and modular in its ability to vary critical quantities that impact the simulated SED. This might include the stellar initial mass function, AGN emission model, and properties of the stellar population synthesis model (such as the inclusion of thermally pulsating asymptotic giant branch stars). Second, a high level of scalability is important. Given ever-increasing mass and spatial resolution in galaxy formation simulations (e.g., Vogelsberger et al. 2014; Schaye et al. 2015; Hopkins et al. 2018; Davé et al. 2019), the ability to run efficient parallelized models is important. Third, there is a need for a portable code that interfaces with disparate galaxy formation models. Many of the existing codes in the literature are optimized for a single hydrodynamic code, making it difficult to compare between different data sets. Comprehensive efforts to compare cosmological and idealized hydrodynamic galaxy formation simulations such as the AGORA comparison project (Kim et al. 2014, 2016) further underscore the need for such a code package.

Motivated by this, as well as our vision for an open-source, community-supported dust radiative transfer package for galaxies, we build off of previous efforts in this work and introduce POWDERDAY. Our principle goals with this code are to develop a lightweight, highly flexible, and modular dust radiative transfer package that interfaces seamlessly with numerous open-source galaxy formation codes. To achieve this, we build POWDERDAY on extremely flexible packages, including FSPS for stellar population synthesis (Conroy et al. 2009, 2010; Conroy & Gunn 2010), HYPERION for the Monte Carlo radiative transfer (Robitaille 2011), and YT for interfacing with galaxy models (Turk et al. 2011).

In this paper, we present the first release of POWDERDAY. We outline the basic algorithms and code methodologies, describe its usage, and present examples highlighting the utility of a flexible dust radiative transfer package. The current code is currently designed to interface seamlessly with outputs from GIZMO (Hopkins 2014, 2017), GASOLINE (Wadsley et al. 2004), CHANGA (Menon et al. 2015), AREPO (Springel 2010), and ENZO (Bryan et al. 2014; Brummel-Smith et al. 2019). Finally, we close with an outlook on future directions for development. POWDERDAY itself is written in Python, though it makes use of Fortran, C, and Cython via dependency software.

## 2. Code Description—Physics

We begin the description of the code by first outlining the underlying physics that goes into the radiative transfer. We follow this in Section 3 with a description of the implementation itself. In Figure 1, we show a schematic of the overall code flow that will serve as a reference throughout both this section and Section 3.

### 2.1. Overview

As a higher-level overview, POWDERDAY projects the physical quantities from hydrodynamic galaxy formation simulations onto an adaptive grid (or uses the underlying mesh, if available), calculates the SED for the luminous sources, and then propagates this light through the dusty ISM. The dust temperatures are calculated self-consistently so that the final result from this are model SEDs from the ultraviolet (longward of 912 Å) through the millimeter wave. In what follows, we outline the details of these calculations. This section is not meant to serve as a user manual but rather an overview of the design and methods. A full user manual can be found at <https://powderday.readthedocs.io/en/latest/>.

### 2.2. Test Model Galaxies

Throughout this paper, we will provide both model tests and examples of the code’s capabilities on a number of different simulation data sets. In Table 1, we summarize these models. In summary, we seek to use a diverse range of hydrodynamic simulation codes as well as simulation types (i.e., idealized, cosmological zoom-in, and bona fide cosmological). We use these throughout this paper in various tests and examples in part to demonstrate the seamlessness with which POWDERDAY interfaces with a diverse range of galaxy formation models. We describe these models briefly here.

1. GIZMODISK is a cosmological zoom-in simulation of a disk-like galaxy at  $z \approx 0$  run by Narayanan et al. (2018a, 2018b), Li et al. (2018), and Privon et al. (2018). This simulation was run with the hydrodynamic

code GIZMO, with the MUFASA suite of galaxy formation physics enabled (Davé et al. 2016).

2. LATTE is a cosmological-zoom in the simulation of a Milky Way-like galaxy from the Latte simulation series. The Latte suite of FIRE-2 cosmological zoom-in baryonic simulations of Milky Way-mass galaxies (Wetzel et al. 2016), part of the Feedback In Realistic Environments (FIRE) simulation project, was run using the GIZMO gravity plus hydrodynamics code in meshless finite-mass (MFM) mode (Hopkins 2015) and the FIRE-2 physics model (Hopkins et al. 2018).
3. GASOLINEDISK is an idealized GASOLINE simulation of a disk-like galaxy, publicly available at <https://yt-project.org/data/>.
4. CHANGAMW is a cosmological zoom-in simulation of a Milky Way-mass galaxy at  $z \sim 0$  performed by Tremmel et al. (2017) and Sanchez et al. (2019) with the CHANGA hydrodynamic code.
5. SMUGGLEDISK is an idealized Milky Way-like disk galaxy run with the AREPO hydrodynamic code by Marinacci et al. (2019), with the SMUGGLE physics suite enabled.
6. TNGHALO is an AREPO simulation of a massive halo from the ILLUSTRIS-TNG simulation and is publicly available in snapshot form at <https://yt-project.org/data/>.
7. ENZODISK is an idealized disk galaxy run with ENZO and publicly available at <https://yt-project.org/data/>.
8. SIMBA M25N512 is a cosmological simulation first run for the study of Narayanan et al. (2018a). This cosmological box employing the SIMBA galaxy formation physics model (Davé et al. 2019; Li et al. 2019) is  $25 h^{-1}$  Mpc on a side.

### 2.3. Grid Construction and Structure

Capitalizing on the flexibility afforded by HYPERION, POWDERDAY is able to perform radiative transfer for hydrodynamic simulations that are particle based, operate on adaptive meshes, and on unstructured meshes.

The radiative transfer happens on a mesh. For particle-based codes, the physical properties of the particles are projected onto an adaptive mesh with an octree memory structure and smoothed utilizing a spline kernel. The hierarchy in the octree is depth first. Formally, the entire data set of particles is encapsulated into a single cell, which then recursively refines into octs until the maximum threshold number of particles are present in a cell.

For codes that operate on a Voronoi mesh (i.e., AREPO), POWDERDAY leverages HYPERION’s ability to perform radiative transfer on the mesh itself and reconstructs the mesh based on the particle positions. Similarly, for adaptive mesh codes (e.g., ENZO), POWDERDAY performs the radiative transfer directly on the grid used for the evolution of fluid quantities in the hydrodynamic simulation.

### 2.4. Stellar Population Synthesis

The stellar clusters in simulations emit SEDs based on their metallicities and ages which are drawn from the galaxy simulations.<sup>18</sup> To calculate these, we leverage the high level of

<sup>18</sup> Sometimes a population of “old stars” is initialized with idealized simulations. For these stars, the ages and metallicities are input as a free parameter.



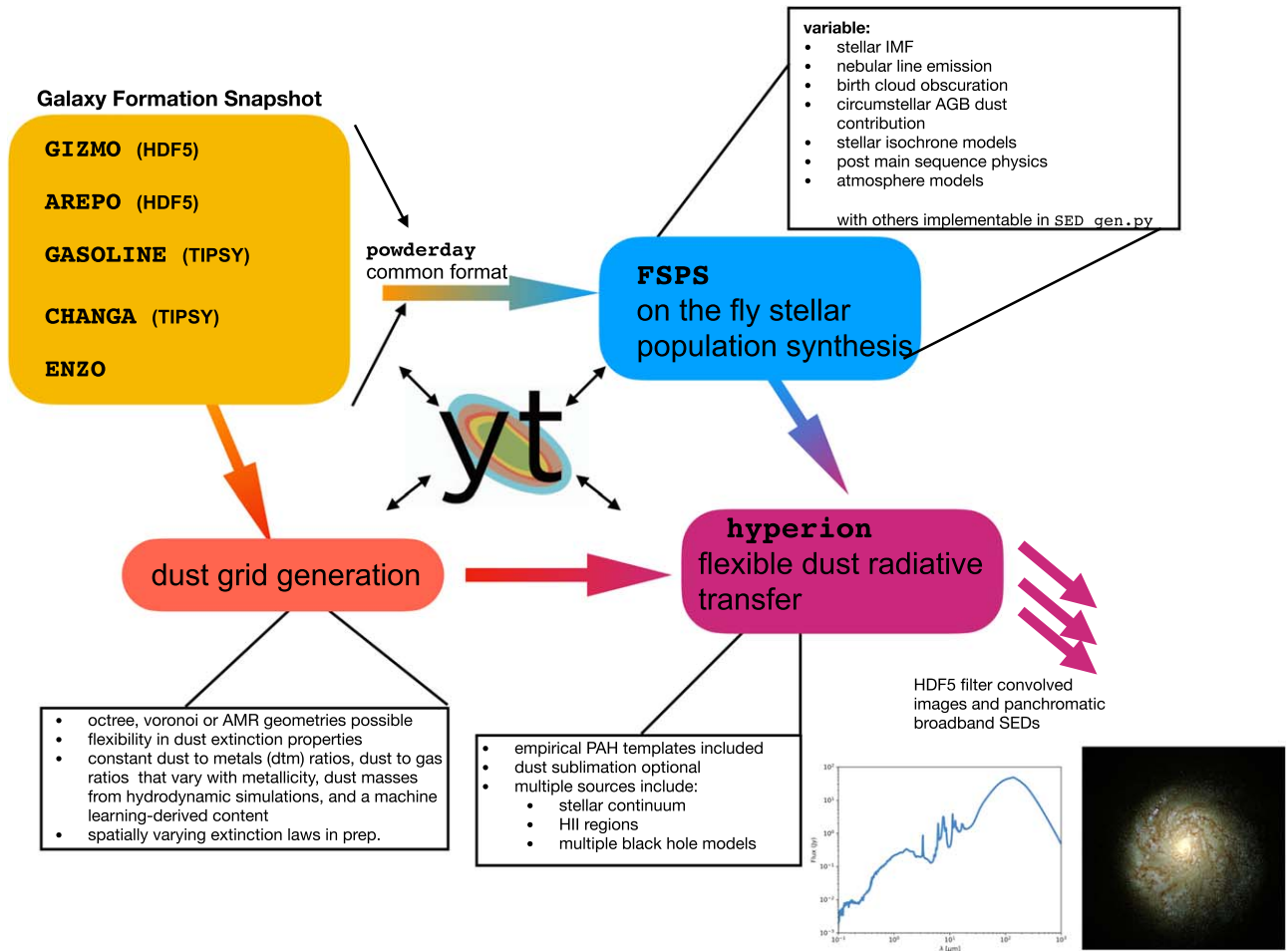


**Figure 1.** Schematic showing a high-level view of the code architecture of POWDERDAY. POWDERDAY interfaces with a broad range of hydrodynamic galaxy evolution codes, regularizing them into a common format. The stellar population synthesis is done on the fly with FSPS and thus offers significant run-time flexibility. Similar levels of flexibility exist with the dust grid generation, including the ability to use the outputs from newer on-the-fly dust evolution models in cosmological simulations. Finally, the dust radiative transfer is performed with the HYPERION Monte Carlo dust radiative transfer code. Throughout the entire code flow, POWDERDAY depends on YT as a glue connecting a wide range of modules.

flexibility available in the FSPS population synthesis code<sup>19</sup> (Conroy et al. 2009, 2010; Conroy & Gunn 2010). The methodology of constructing a stellar population synthesis is covered in the aforementioned papers, as well as the reviews by Walcher et al. (2011) and Conroy (2013), and we refer the reader to these works for detailed discussion.

This level of flexibility adds a powerful dimension to POWDERDAY currently unavailable in any other public dust radiative transfer package. In principle, nearly any population synthesis option available in FSPS is also available for variation in POWDERDAY. In practice, the default version of the code ships with the ability to handle variable functional forms for the stellar IMF (with both relatively standard options available such as Salpeter 1955, Chabrier 2003, and Kroupa 2002, and user-specified IMFs), a range of theoretical isochrones (e.g., Schaller et al. 1992; Bertelli et al. 1994; Pietrinferni et al. 2004), varying contributions to the SED from post-AGB stars, a circumstellar AGB dust model, obscuration of young stars by unresolved birth clouds, and nebular line emission (as we will discuss in Section 2.5, both building off of

the FSPS libraries developed by Byler et al. 2017, 2018, 2019, as well as via direct CLOUDY modeling). A key point here is that because FSPS is actively being developed and maintained, new features developed in this population synthesis code will also be available in POWDERDAY.

Stellar sources are currently included as point sources. Future versions of the code will smooth their emission in a kernel-weighted manner, using information about the particle smoothing lengths from the galaxy formation simulation itself.

### 2.5. Nebular Line Emission

POWDERDAY includes nebular line emission from H II regions around massive stars using CLOUDY calculations. These come in two flavors: lookup tables (that are relatively efficient), and slower but more flexible direct CLOUDY models that are run on the fly. Because both methods tie the nebular line emission to the star particles themselves, these lines are attenuated by any diffuse dust they see as they exit the galaxy.

The first method uses CLOUDY lookup tables generated for FSPS stellar population synthesis models developed by Byler et al. (2017, 2018, 2019). These lookup tables, computed with CLOUDY V13.03 are built for a grid of stellar age ( $t_{\text{age}}$ ), metallicity ( $Z$ ), and ionization parameter which range from  $-4 \leq \log_{10} U \leq -1$ ,  $-1.98 \leq \log_{10} Z_{\text{H II}} \leq 0.198$ , and

<sup>19</sup> On a practical level, in order to interface with the Fortran-based FSPS, we utilize the publicly available FSPS Python hooks originally developed by D. Forman-Mackey (<http://dan.iel.fm/python-fsps>).

**Table 1**  
Model Simulations Used in This Paper

Name	Type of Simulation	Type of Galaxy	Snapshot Type	Snapshot Location	Citation
GIZMODISK	Cosmological Zoom	$z = 0$ Disk	GIZMO HDF5	<sup>a</sup>	Narayanan et al. (2018a, 2018b)
LATTE	Cosmological Zoom	$z = 0$ Disk	GIZMO HDF5	<sup>b</sup>	Hopkins et al. (2018)
GASOLINEDISK	Idealized	Isolated Disk	GASOLINE TIPSy	<sup>c</sup>	Wetzel et al. (2016)
CHANGAMW	Cosmological Zoom	$z = 0$ Disk	CHANGA TIPSy	<sup>d</sup>	Sanchez et al. (2019)
SMUGGLEDISK	Idealized	Isolated Disk	AREPO HDF5	<sup>e</sup>	Tremmel et al. (2017)
TNGHALO	Cosmological	Galaxy Cluster	AREPO HDF5	<sup>f</sup>	Marinacci et al. (2019)
ENZODISK	Idealized	Isolated Disk	ENZO	<sup>g</sup>	Pillepich et al. (2018)
SIMBA M25N512	Cosmological	N/A	GIZMO HDF5	<sup>h</sup>	Kim et al. (2014)
					Davé et al. (2019)

<sup>a</sup> [https://users.astro.ufl.edu/~desika.narayanan/powderday\\_files/mufasa\\_gizmo\\_snapshot\\_134.hdf5](https://users.astro.ufl.edu/~desika.narayanan/powderday_files/mufasa_gizmo_snapshot_134.hdf5)

<sup>b</sup> <https://fire.northwestern.edu/>

<sup>c</sup> <http://yt-project.org/data/TipsyGalaxy.tar.gz>

<sup>d</sup> [https://users.astro.ufl.edu/~desika.narayanan/powderday\\_files/changa\\_starform\\_example](https://users.astro.ufl.edu/~desika.narayanan/powderday_files/changa_starform_example)

<sup>e</sup> [https://users.astro.ufl.edu/~desika.narayanan/powderday\\_files/smuggle\\_snapshot\\_143.low\\_res.hdf5](https://users.astro.ufl.edu/~desika.narayanan/powderday_files/smuggle_snapshot_143.low_res.hdf5)

<sup>f</sup> <http://yt-project.org/data/TNGHalo.tar.gz>

<sup>g</sup> <http://yt-project.org/data/IsolatedGalaxy.tar.gz>

<sup>h</sup> Available by request.

$0.5 \leq t_{\text{age}} \leq 20$  Myr. Here, the ionization parameter is the usual dimensionless ratio between the number of ionizing photons and hydrogen density:

$$U_0 \equiv \frac{Q_{\text{H}}}{4\pi R_{\text{H II}}^2 \times n_{\text{H, H II}} \times c}, \quad (1)$$

where  $Q_{\text{H}}$  are the total number of hydrogen ionizing photons emitted per second:

$$Q_{\text{H}} \equiv \frac{1}{hc} \int_0^{912 \text{ \AA}} \lambda f_{\lambda} d\lambda, \quad (2)$$

$n_{\text{H, H II}}$  is the density of the H II region, and is assumed to be fixed at  $n_{\text{H, H II}} = 100 \text{ cm}^{-3}$ .  $R_{\text{H II}}$  is the radius of the H II region. The formal definition for  $U$  uses the Strömgren radius. However, this is only known after the photoionization state is computed! Therefore,  $R_{\text{H II}}$  is set to  $R_{\text{H II}} = R_{\text{inner, H II}}$ , which is the inner boundary of the H II region, and the quantity of interest for the CLOUDY calculations. Byler et al. (2017) assume  $R_{\text{inner}} = 10^{19} \text{ cm}$ .

POWDERDAY additionally includes a number of options relevant to nebular line emission from the H II region relevant to galaxy-wide radiative transfer. First, many simulations (especially cosmological ones) have mass resolutions that are significantly larger than the mass of a typical stellar cluster. This can lead to unphysically large ionization parameters,  $U_0$ , owing to the increased number of Lyman-limit photons. We therefore allow the user to subdivide stellar particles into a mass spectrum of stellar clusters following a power-law function:

$$\frac{dN}{dM} \propto M^{\beta} \quad (3)$$

based on observational constraints by Chandar et al. (2014, 2016). Each of these clusters then radiates its own individual SED, though are assumed to be cospatial at the point of the parent star particle. Second, while  $U$ ,  $Q$  and the metallicity of the H II region ( $Z_{\text{H II}}$ ) are all calculated based on the particle properties, it is conceivable that the user may

wish to hold these fixed as an assumed value, and can therefore be set by the user.

Alongside lookup tables, POWDERDAY allows for the direct computation on the fly of nebular line emission from all stars (or stars within certain age thresholds for computational ease). For these, we couple the simulations to CLOUDY (Ferland et al. 2013). This offers significant advantages over the aforementioned lookup-table-dependent methods as it obviates the need for the user to have to generate new lookup tables for every new set of assumed stellar parameters. For these calculations, we assume a spherical H II region geometry in which the inner boundary of the H II region is user settable to some fraction  $\zeta$  of the Strömgren radius:

$$R_{\text{inner}} = \zeta R_{\text{S}} = \zeta \left( \frac{3Q_{\text{H}}}{4\pi n_{\text{H}}^2 \alpha_{\text{B}}} \right)^{1/3}, \quad (4)$$

where the  $n_{\text{H}}$  has a default value of  $100 \text{ cm}^{-3}$ , and the temperature of the region has a default value of  $T = 10^4 \text{ K}$  for the calculation of  $Q_{\text{H}}$  (though both are adjustable).

While the direct calculation of emission from H II regions on a particle by particle basis can be slow, it offers two distinct advantages over the lookup tables. First, there is a significant flexibility advantage. For example, if a user wants to include dust in H II regions using lookup tables, they would have to completely regenerate the lookup table. When employing CLOUDY on the fly, it is straightforward to simply update this in the CLOUDY parameter file and re-run the POWDERDAY simulation. Second, as previously mentioned, the lookup tables are parameterized in a grid of stellar age, metallicity, and ionization parameter, where the resulting nebular line emission for a given star particle is interpolated within this grid. By employing the direct CLOUDY simulations on a particle by particle basis, one is able to avoid this interpolation, which can impact the expected fluxes from individual lines.

In Figure 2, we show an example of the nebular line models in our simulations. We show the UV-optical SED of model galaxy GIZMODISK in three cases: with nebular line emission turned off and with the nebular line emission calculated via the Byler et al. (2017) lookup tables and via direct CLOUDY

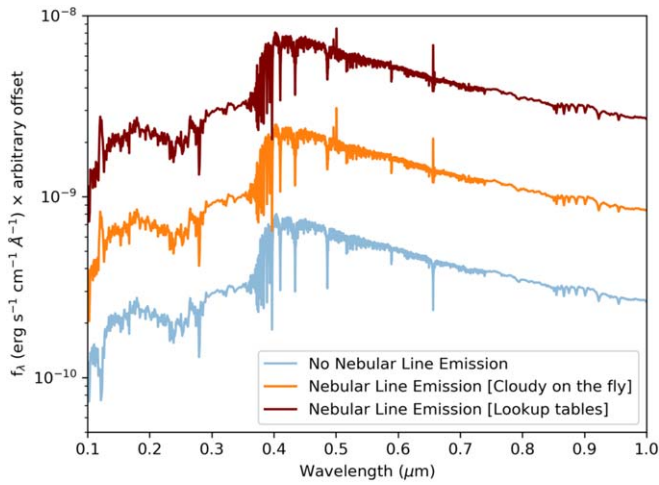


**Figure 2.** Impact of nebular line emission on UV-optical SED of a star-forming galaxy (model GIZMODISK). The blue line shows the default model with no nebular line emission, the orange line shows the UV-optical SED (including nebular lines) for a model in which the spectrum from photoionization regions around young stars are calculated with on the fly CLOUDY models, while the maroon line shows the same, but with the nebular line emission computed via the Byler et al. (2017) lookup tables. The flux densities (ordinate) are offset by an arbitrary multiplicative to aid in clarity.

calculations. The largest impact to the UV-optical SED obviously occurs when comparing a model with no emission from H II regions versus a model that includes it: the addition of H II regions to the source term contributes to both continuum and line emission in the UV/optical. While the model using lookup tables is fairly similar to that using CLOUDY on the fly, there are of course quantifiable differences in the line and continuum strength. These primarily owe to the interpolation in (ionization parameter, stellar age, metallicity) space for the lookup tables versus direct calculation.

Finally, we note that any of the features available in CLOUDY are in principle available to our models that employ direct CLOUDY simulations. This said, one must be careful, as some choices can drive unphysical effects. One clear example is the inclusion of nebular dust. While H II region dust may at times be an important source of infrared luminosity in some bands, POWDERDAY does not currently include the capability of “borrowing” this dust from the nearest grid cell. This means that if H II region dust contributes significantly to the total dust mass in this example, one runs the risk of double counting some dust mass near massive stars.

### 2.6. Active Galactic Nuclei

Radiation from accreting black holes can also be included in POWDERDAY. We assume that the luminosity of the black hole is proportional to the mass accretion rate, modulated by an efficiency parameter  $\eta$ :

$$L_{\text{AGN}} = \eta \dot{M}_{\text{BH}} c^2, \quad (5)$$

where  $L_{\text{AGN}}$  is the black hole luminosity,  $\dot{M}_{\text{BH}}$  is the black hole accretion rate, and  $c$  is the speed of light. The template spectrum for the AGN is based on the luminosity-dependent templates of observed unreddened type 1 quasars (Hopkins et al. 2007). Hot dust emission from the putative torus is included in the template and is based on the mid-IR SED

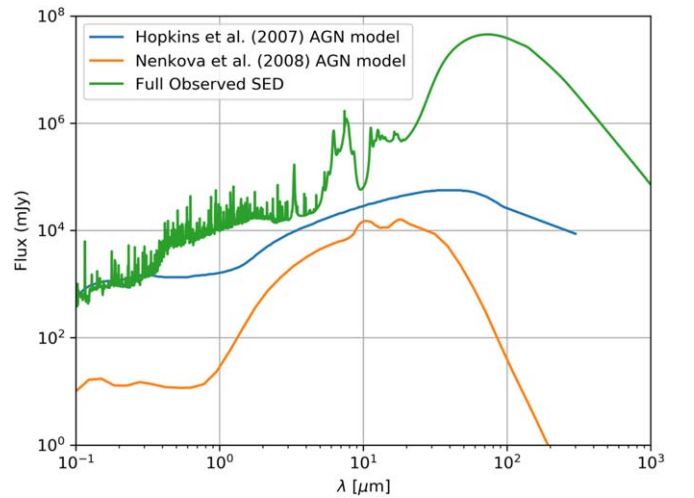


**Figure 3.** Example of possible input SEDs for accreting black holes. The blue line shows the Hopkins et al. (2007) template SED, while the orange line shows the Nenkova et al. (2008b) model. The green line shows the output observed SED (including the contribution from stars and dust).

template of Richards et al. (2006). The normalization of this template is based on the bolometric luminosity for the AGN, given by Equation (5), and the efficiency  $\eta$  is a free parameter.

As an alternative to the Hopkins et al. (2007) AGN SED templates, POWDERDAY also includes the option to employ the CLUMPY SED templates from Nenkova et al. (2008a, 2008b). CLUMPY models an inhomogeneous dust-obscuring structure around the AGN and provides a grid of SED templates that include torus-scale dust obscuration and emission. The dust structure is fully described by the dust optical depth ( $\tau_V$ ), torus inclination ( $i$ ), number of dust clumps along the line of sight ( $N_0$ ), and the angular and radial spatial distributions of the clumps ( $Y, q, \sigma$ ). The dust grains are assumed to have the optical properties of a standard Milky Way mixture, which Nenkova et al. (2008b) find agree with observed AGN dust compositions. Clumpy dust structures provide a potential explanation for the observed behavior of  $10 \mu\text{m}$  silicate absorption in AGNs (Mason et al. 2006), as well as the compact size of the torus (Poncellet et al. 2006), the close spatial proximity of vastly different dust temperatures within AGN (Schartmann et al. 2005), and broad-line emission at equatorial viewing angles (Alonso-Herrero et al. 2003).

In Figure 3, we show an example model demonstrating how the Hopkins et al. (2007) and Nenkova et al. (2008b) AGN models are included. The modeled galaxy is an arbitrarily chosen one (galaxy #12) from the SIMBA m25n512 simulation. The solid green line is the output observed SED, while the blue and orange lines show the input model AGN SEDs (of course, in a realistic run only a single model would be employed at a time). For the Nenkova et al. (2008b) template, we assume a default set of parameters of  $[N_0, Y, i, q, \sigma, \tau_V] = [5, 30, 0, 1.5, 30, 40]$ .

Finally, POWDERDAY includes the option to apply post-processed, short-timescale AGN variability using the analytic prescription from Hickox et al. (2014). This prescription gives the relative time,  $t$ , spent by an AGN at a given fraction of its bolometric luminosity,  $L_{\text{rel}}$ . It takes the form of a Schechter function with an exponential cutoff at  $L_{\text{cut}} = 100L_{\text{AGN}}$  and a



lower limit of  $10^{-5}L_{\text{AGN}}$ :

$$\frac{dt}{d \log L_{\text{rel}}} = t_0 \left( \frac{L_{\text{rel}}}{L_{\text{cut}}} \right)^{-\alpha} \exp(-L_{\text{rel}}/L_{\text{cut}}), \quad (6)$$

where the characteristic timescale,  $t_0$ , is adjusted such that the integral over all  $L_{\text{AGN}}$  is 1. We use the Hickox et al. (2014) fiducial model with the power-law slope  $\alpha = 0.2$ , which they find gives a robust compromise between observed Eddington ratio distributions (Hopkins & Hernquist 2009; Kauffmann & Heckman 2009) and simulated AGN variability (Novak et al. 2011). Hickox et al. find that applying short-timescale variability to observations reproduces general trends in AGN luminosity functions and merger fractions, and yields a close connection between AGN activity and SFRs over galaxy evolution timescales. For each simulation snapshot, we sample the prescribed luminosity distribution, vary the black hole bolometric luminosity according to the drawn relative luminosity, then continue the radiative transfer.

### 2.7. Cosmic Microwave Background (CMB)

The CMB is included as an additional energy density term in every cell in the simulation. Specifically, we model this as

$$\epsilon = \int \kappa_\nu B_\nu d\nu \text{ erg s}^{-1} \text{ g}^{-1}, \quad (7)$$

where  $\kappa_\nu$  is the dust absorption opacity (based on the assumed extinction properties of the dust grains) and  $B_\nu$  is the Planck function. As demonstrated by Privon et al. (2018), this heating term can be nonnegligible for high-redshift ( $z \gtrsim 4-5$ ) galaxies.

### 2.8. Dust Content

For all types of grids, the fundamental quantity of interest for the radiative transfer is the dust density, which can be specified in a number of ways. To specify the dust content in a given grid cell, we include both observationally motivated and theoretically motivated methods for determining the dust mass. The simplest and most traditional method for determining the dust mass is to employ a constant dust mass to metals mass ratio. Indeed, a relatively narrow range of values has been reported by a number of authors over a diverse range of galaxy environments and redshifts (e.g., Dwek 1998; Vladilo 1998; Watson 2011). Alternatively, recent observations by Rémy-Ruyer et al. (2014) and De Vis et al. (2019) have demonstrated a trend between the dust-to-gas ratio and metallicity of galaxies. Accordingly, we include this scaling (specifically, the best-fit single power-law relation by Rémy-Ruyer et al. 2014, in which the CO–H<sub>2</sub> conversion factor is allowed to vary with metallicity).

Similarly, advances in galaxy formation algorithms in the last few years have ushered in a new suite of models that include on-the-fly dust formation, growth, and destruction processes (e.g., Asano et al. 2013; McKinnon et al. 2016, 2018; Aoyama et al. 2017, 2018; Hou et al. 2017, 2019; Popping et al. 2017b; Li et al. 2019). For these types of simulations, POWDERDAY can explicitly read in the dust masses from the simulation themselves, offering self-consistency with the galaxy formation simulation.

Finally, we include the option of generating dust masses by leveraging the capabilities of simulations that include on the fly dust physics, even for galaxy models that do not include dust

physics. To do this, we employ the results of Li et al. (2019), which uses the SIMBA dust formation, growth, and destruction framework to map the physical properties of galaxies to their dust content. We provide two options from the Li et al. (2019) model. The first is an approximate mapping between the dust-to-gas ratio (DGR) and the gas-phase metallicity:

$$\log \text{DGR} = 2.445 \times \left( \frac{Z}{Z_\odot} \right) - 2.029. \quad (8)$$

This relation carries two sources of uncertainty with it. First, similar to the observational work of Rémy-Ruyer et al. (2014), which reports a similar mapping, Equation (8) is constructed for galaxy-wide scales, which therefore provides a similar uncertainty to employing the Rémy-Ruyer et al. (2014) relations when applying these relations to resolved scales within galaxies (i.e., on a particle-by-particle or cell-by-cell basis). The second uncertainty folded into Equation (8) is that there is significant scatter associated with this mapping. A primary result of Li et al. (2019) was that there are numerous secondary dependencies between the dust-to-gas ratio and physical properties of galaxies beyond the gas-phase metallicity that, when included in the mapping, can significantly reduce the scatter.

To move beyond these two sources of uncertainty, Li et al. (2019) developed a machine-learning framework to map between the DGR of galaxies and their physical properties, thereby reducing the scatter intrinsic in the single parameter mapping between DGR and  $Z$ . To inform dust mass calculations on resolved scales for POWDERDAY, we build on the Li et al. (2019) model and provide a mapping between the DGR and metallicity, SFR, and gas mass of every particle in the SIMBA-100 (100 Mpc)<sup>3</sup> cosmological simulation at redshift  $z = 0$ . This mapping utilizes the Extremely Randomized Trees method within the SCIKIT-LEARN software package. The advantage of this model is that it allows modelers who do not otherwise have information about the dust content of their galaxy to take advantage of results from simulations that do, thereby allowing for increased sophistication over more typical constant dust-to-metals ratio assumptions.

In Figure 4, we show the impact of these different dust model choices on a calculated SED (from galaxy 9 in the  $z = 0$  snapshot of the SIMBA m25n512 simulation). It is important to note that this model is simply an example (and indeed the galaxy was chosen arbitrarily) and not representative of all model galaxies. With this in mind, we see that the biggest impact is on both the UV radiation, as well as the mid-FIR SED. Factors of  $\sim 2-4$  differences in the attenuated UV flux alone can be ascribed solely to the implemented dust model, though again, we caution that this is simply an example and a statement of the exact uncertainty one might expect in any given radiative transfer calculation.

### 2.9. Polycyclic Aromatic Hydrocarbons

We follow the methodology of Robitaille et al. (2012) for including polycyclic aromatic hydrocarbons (PAHs) as they are modeled in HYPERION. The PAH model is based on a modified version of the Draine & Li (2007) model. We utilize the Draine & Li (2007) emissivities and opacities for dust grains, though bin the grains into three size distributions: ultra-small grains (USGs;  $a < 20 \text{ \AA}$ ), very small grains (VSGs;

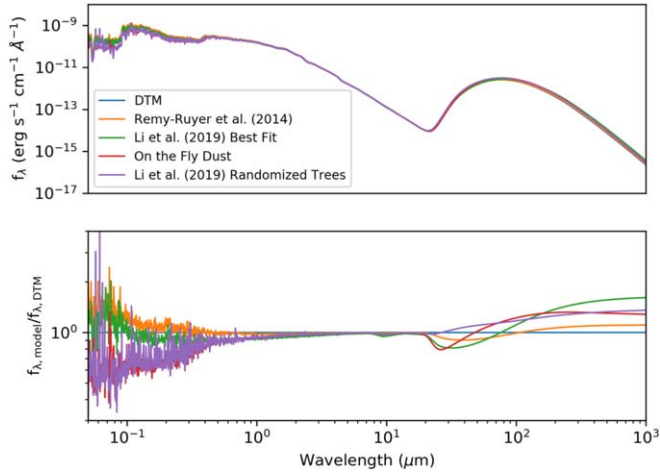


**Figure 4.** Impact of different choices for modeling dust on derived SEDs. We investigate modeling the dust via a simple dust-to-metals ratio (DTM), following the Rémy-Ruyer et al. (2014) observational scaling with metallicity on galaxy-wide scales, using the Li et al. (2019) best-fit relation between the dust-to-gas ratio and metallicity from simulated galaxies, an explicit on-the-fly dust calculation, and via the Li et al. (2019) machine-learning framework. In the top panel, we show the actual SEDs from these models, and in the bottom panel, the relative errors. The model employed here was GALAXY9 from the  $z = 0$  snapshot of the m25n512 SIMBA simulation.

$20 \text{ \AA} < a < 200 \text{ \AA}$ ), and big grains ( $a > 200 \text{ \AA}$ ). Here, the PAHs are assumed to be exclusively in the smallest (USG) bin, while the grains in the largest bin follow the adopted global grain size distribution (i.e., Weingartner & Draine (2001)). The distribution of USGs, VSGs, and big grains can be set by the user, though they have a default proportion of 5.86%, 13.51%, and 80.63%, respectively.

Traditionally, the dust emissivities in the Draine & Li (2007) formalism are computed for variable radiation intensities, scaled by the interstellar radiation field in the solar neighborhood as computed by Mathis et al. (1983). As discussed in Robitaille et al. (2012), HYPERION instead parameterizes the radiation field by the power absorbed by grains, which accounts for differing spectral shapes. The dust emissivities are computed for bins of power of radiation field absorbed by the grains per unit mass:

$$\dot{A} = \int 4\pi J_{\text{isrf}} \kappa_{\nu} d\nu, \quad (9)$$

where  $J_{\text{isrf}}$  is the mean intensity of the radiation field at the location of the dust grain.

In Figure 5, we demonstrate the impact of the USG fraction on the PAH emission intensity via an example SED (model LATTE) in which we run with our default USG/VSG/big grain setup, as well as by incrementally halving the USG mass fraction. As the USG fraction decreases, the UV flux density increases as the power in the PAHs commensurately decreases. Currently, this mass fraction of grains in PAHs is a free parameter, though future versions of POWDERDAY will have the capability to include an actively modeled size spectrum of dust grains (e.g., Asano et al. 2013; Hirashita 2015; Nozawa et al. 2015; Aoyama et al. 2018; Gjergo et al. 2018; McKinnon et al. 2018; Hirashita & Aoyama 2019; Hou et al. 2019; Q Li et al. 2020, in preparation).

### 2.10. Dust Radiative Transfer

The radiation emitted from luminous sources is then allowed to propagate through the dusty ISM, where the dust masses are

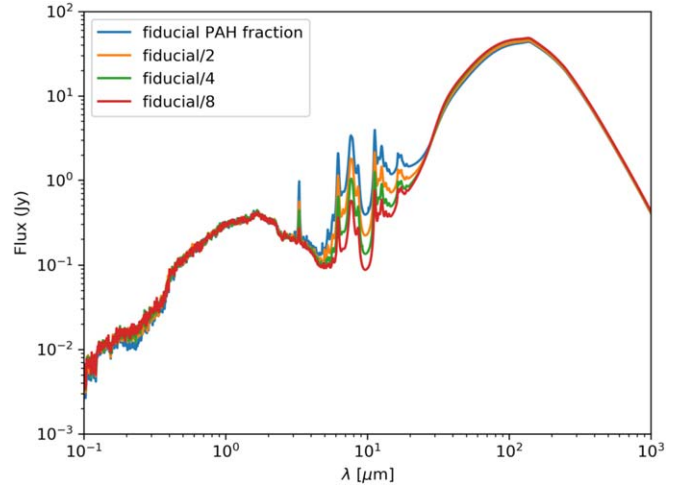


**Figure 5.** Model SED from example galaxy LATTE with decreasing ultra-small grain (USG) mass fraction. The reduced fractions of USGs modify both the UV continuum, as well as the PAH intensity. See the text for details.

computed as described in Section 2.8. These photons propagate through the grid cells and can be scattered, absorbed (and reemitted), or pass through freely. This continues until the photons leave the grid.

We utilize HYPERION as the central dust radiative transfer solver (Robitaille 2011). HYPERION is an ultra-flexible code that solves for the transfer in a Monte Carlo fashion, and utilizes the Lucy (1999) iterative method for determining the equilibrium dust temperature. We note that in what follows, we describe HYPERION as it is used as a part of POWDERDAY. The code contains significantly more options and nuance than is described here, and we refer the reader to Robitaille (2011) for a more detailed description.

We add sources as point sources, with a given SED shape and luminosity. In order to reduce memory overhead, we bin the sources in age and metallicity. Without such a procedure, adding all of the stellar clusters from even a relatively low mass-resolution galaxy simulation would be prohibitive. When included, black holes are added in the same manner as stellar clusters. Photons are randomly sampled from sources, with numbers proportional to the source luminosity. The direction and frequency are randomly drawn, and the photon is propagated until it either escapes the grid or reaches an arbitrary optical depth,  $\tau$ , where  $\tau$  is randomly drawn from the exponential distribution  $e^{-\tau}$ . Formally,  $\tau = -\ln \xi$ , where  $\xi = [0, 1]$ . Whether the photon is absorbed or scattered at this point is dependent on the dust albedo.

The equilibrium dust temperature<sup>20</sup> is calculated iteratively until convergence. This is because the emissivity depends on the mean radiation field, which depends on the emissivity. The iteration continues until a threshold number of cells have differences in specific energy absorption rates below a defined value, and their values have changed by less than a relative threshold value.

SEDs and images are calculated via ray tracing. The source function is determined at each position in the grid, and then the radiative transfer equation is integrated along lines of sight. The SEDs comprise wavelengths where radiation is emitted (though bounded by the wavelengths of dust opacity tables). Images are

<sup>20</sup> In practice what is calculated is the equilibrium dust emissivity and mean opacity, which are functions of temperature.



made only at prespecified wavelengths in order to save on memory cost.

### 3. Code Description—Implementation

#### 3.1. Front Ends

In order to aid in user ease, POWDERDAY leans on YT for reading in galaxy snapshots. POWDERDAY reads in individual snapshots as a YT data set object, and therefore has all of the associated methods and attributes offered in YT available to it. The simulation type is automatically detected within YT and passed to the appropriate POWDERDAY front end, which converts the unique field names and units associated with each simulation type to internal ones so that downstream from the front end, all physics in the code remains the same, regardless of the input hydrodynamic simulation. Currently, front ends exist for GIZMO, GASOLINE, CHANGA, AREPO and ENZO.

#### 3.2. Code Scaling

POWDERDAY is a parallelized code that offers reasonable scaling with processor number. The code is fundamentally broken into two regimes: the stellar population synthesis and model setup, and the radiative transfer. The most costly aspect of the model setup is the SED generation. As a result, this is parallelized via the POOLMAP multithreading package in Python. The radiative transfer in HYPERION is fully MPI parallelized. What this means is that there is a fixed overhead for a given problem in generating the stellar population and other model setup procedures, while the radiative transfer itself represents a highly scalable parallel problem. How the problem scales will depend in part on the computer configuration. The SED generation can operate on many tasks on a single compute node, whereas the radiative transfer can employ multiple networked nodes. As a result, the optimal configuration for parallelization is to employ many tasks on a single compute node: this allows for both the stellar SED generation and the radiative transfer to be maximally parallelized. Spreading a given POWDERDAY simulation across many nodes will lose some efficiency as the initial SED generation will still only occur on a single node.

In Figure 6, we present the result of a scaling test with model SMUGGLEDISK, in which we increase both the number of processors, as well as the number of photons. The solid lines show the actual code performance, while the dashed lines show the ideal scenario (i.e., a scaling that decreases as  $t \sim 1/N_{\text{proc}}$ , where  $t$  is the wall clock time and  $N_{\text{proc}}$  is the number of processors. These tests were performed on a single 32 core node. The combination of the fixed overhead costs and the highly scalable Monte Carlo radiative transfer is apparent in Figure 6: as the problems become increasingly difficult and spend more relative time in the radiative transfer, their scaling approaches the ideal limit.

#### 3.3. Code Comparisons

In this section, we present code comparisons between POWDERDAY and SKIRT. SKIRT (Baes et al. 2011; Baes & Camps 2015; Camps & Baes 2015, 2020; Verstocken et al. 2017) is a state-of-the-art open-source code designed to perform continuum radiative transfer in dusty systems that have been widely used. For these tests, we design SKIRT models to mimic as closely as possible POWDERDAY models

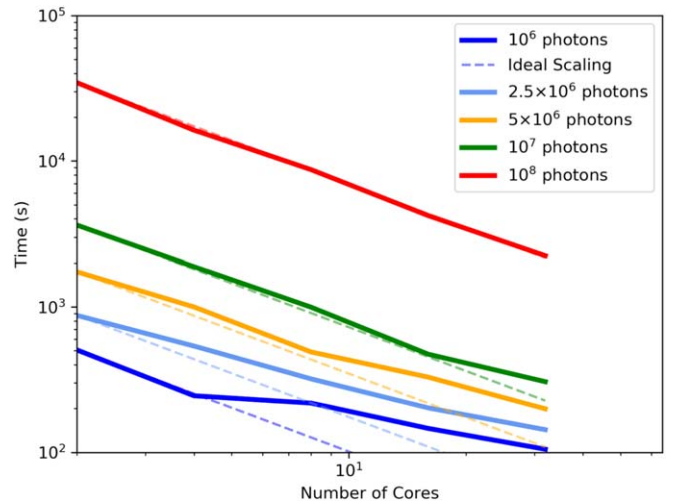


**Figure 6.** Scaling tests for POWDERDAY presented as wall clock time as a function of the number of cores for problems of increasing difficulty (parameterized by the total number of photons emitted). POWDERDAY generally shows strong scalability, though, at low photon-count (i.e., easy) problems, the fixed overhead costs in the preradiative transfer stage can drive some inefficiencies.

for code comparison. This said, we caution though that due to differences in the stellar population synthesis models, dust models, and grid construction, a true apples-to-apples comparison is currently intractable given the design of both codes. We employ a Kroupa et al. (1993) stellar initial mass function. The dust is distributed with a constant dust-to-metals ratio of 0.25 with Draine (2003) opacities ( $R_V = 3.1$ ). The contribution of PAHs and nebular lines is turned off.

The galaxy models used for this comparison are GIZMODISK, GASOLINEDISK, CHANGAMW, and TNGHALO. Note, for the AREPO comparison, the SKIRT model was run with the dust geometry distributed in an octree mesh due to technical difficulties with SKIRT, while the POWDERDAY simulation was run over a reconstructed Voronoi grid tessellated about the gas points.

In Figure 7, we show a comparison between the POWDERDAY and SKIRT SEDs for these models. The galaxies are all set at a distance of 1 Mpc for this comparison. While there are some subtle differences that owe to the differing intrinsic stellar population models, as well as dust grid construction, by and large the comparison between the two codes reveals consistent results across the modeled wavelength range. The large degree of correspondence between POWDERDAY and SKIRT for these model tests is encouraging.

#### 3.4. SEDs and Images

As an example of the output of POWDERDAY, in Figures 8 and 9, we show the model SED and multiwavelength images for a range of inclination angles for model LATTE. The galaxy model is a zoom-in of a Milky Way-like galaxy (Wetzel et al. 2016), and the radiative transfer is performed assuming a Kroupa (2002) IMF, a dust-to-metals mass ratio of 40%, and PAH emission turned on.

The SEDs and images are generated over nine viewing angles. In Figure 8, we show the viewing-angle dependence of the SEDs, with more edge-on views naturally resulting in reduced UV/optical flux. The images are generated at the monochromatic wavelengths  $\lambda = [0.5, 1, 30, 100] \mu\text{m}$  and are

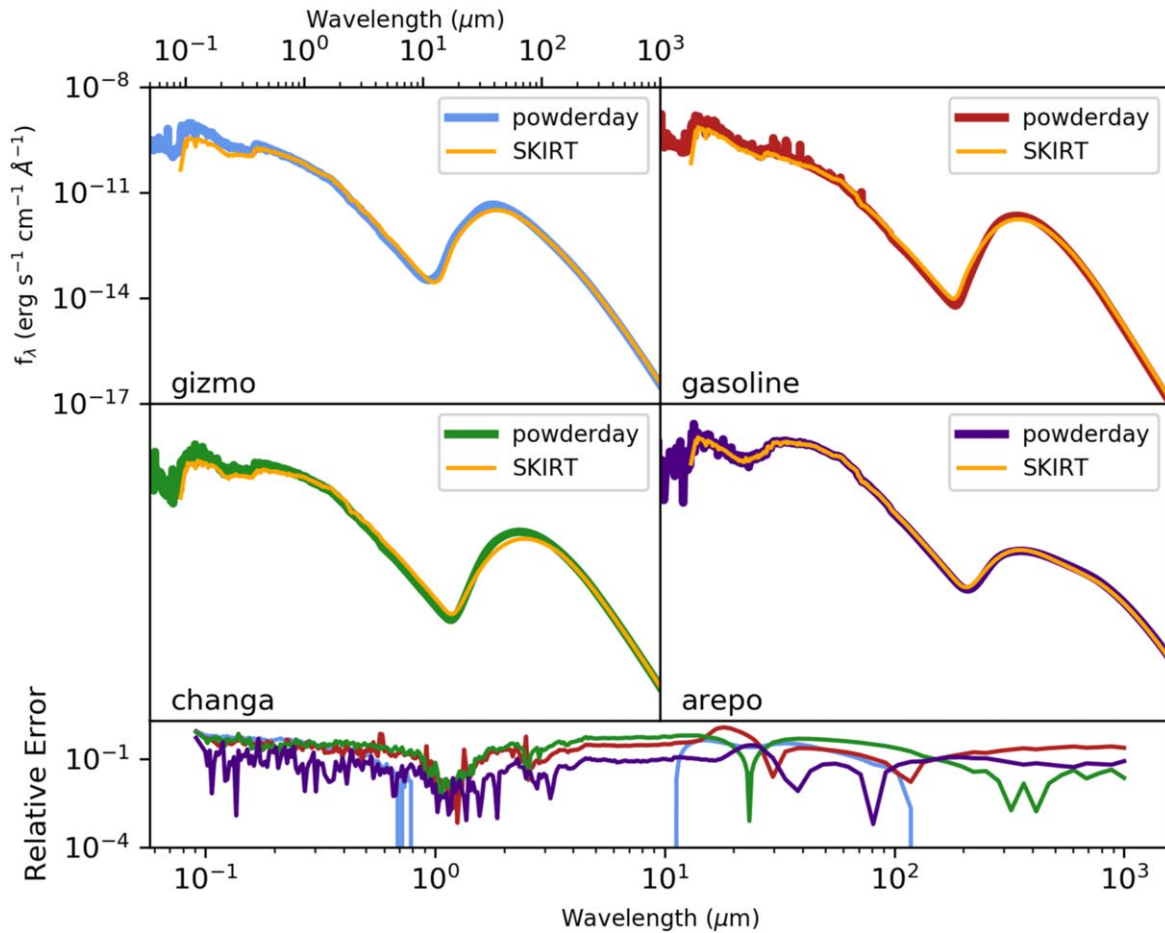


**Figure 7.** Model comparison between POWDERDAY and SKIRT for GIZMO, GASOLINE, CHANGA, and AREPO simulations. The SKIRT run is orange in each panel, and the POWDERDAY run varies in color from model to model (it is this color that denotes which model is which in the bottom panel that shows the relative error). While there are differences in the inherent stellar SED models, as well as the grid construction, the high level of agreement between the output of the two simulation codes is striking.

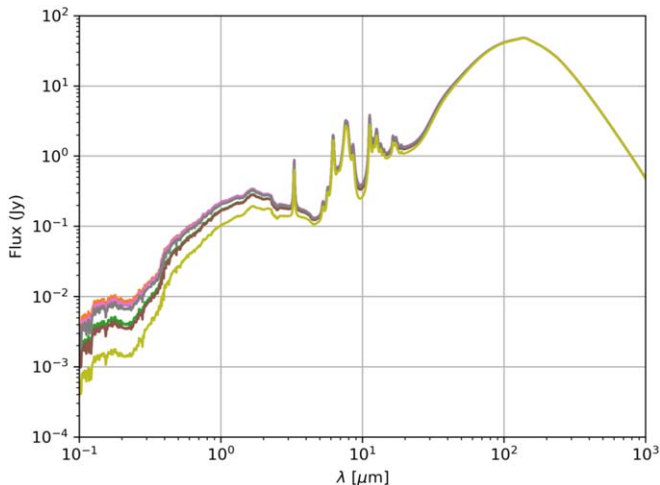


**Figure 8.** Example panchromatic SED from cosmological zoom-in of the Milky Way-like galaxy LATTE (Wetzel et al. 2016). The different lines denote different viewing angles for the galaxy set at 30 Mpc.

shown at three different viewing angles. The images are set at a fiducial distance of 30 Mpc. In the optical/NIR, the face-on views highlight the stellar emission, though with clear dust lanes in the spiral arms that become more prominent as the angles shift toward being edge on. These dust lanes become

significantly more prominent in Figure 10, where we show the simulated RGB colors of the same model galaxy (corresponding to 0.3, 0.5, and 1  $\mu\text{m}$ ). We follow the pipeline of Snyder et al. (2015a) in generating these images, which uses the scaling techniques described in Lupton et al. (2004).

Generally, POWDERDAY can generate images at any number of arbitrary wavelengths. While the images in Figure 9 are not filter convolved, POWDERDAY ships with a number of canned transmission filters and can generate filter-convolved images.

### 3.5. Citing the Code

Fundamentally as a package, POWDERDAY simply wraps FSPS (Conroy & Gunn 2010; Conroy et al. 2010), HYPERION (Robitaille 2011), YT (Turk et al. 2011), and ASTROPY (Astropy Collaboration et al. 2013). We therefore request that any users of the code cite these codes and papers first and foremost, before citing this paper.

## 4. Applications

In what follows, we demonstrate a number of examples and science applications of POWDERDAY. Most of the results presented in this section have already been the subject of complementary work in the literature. These are not meant to be interpreted either as novel results nor deep scientific investigations, but rather examples of the usage of

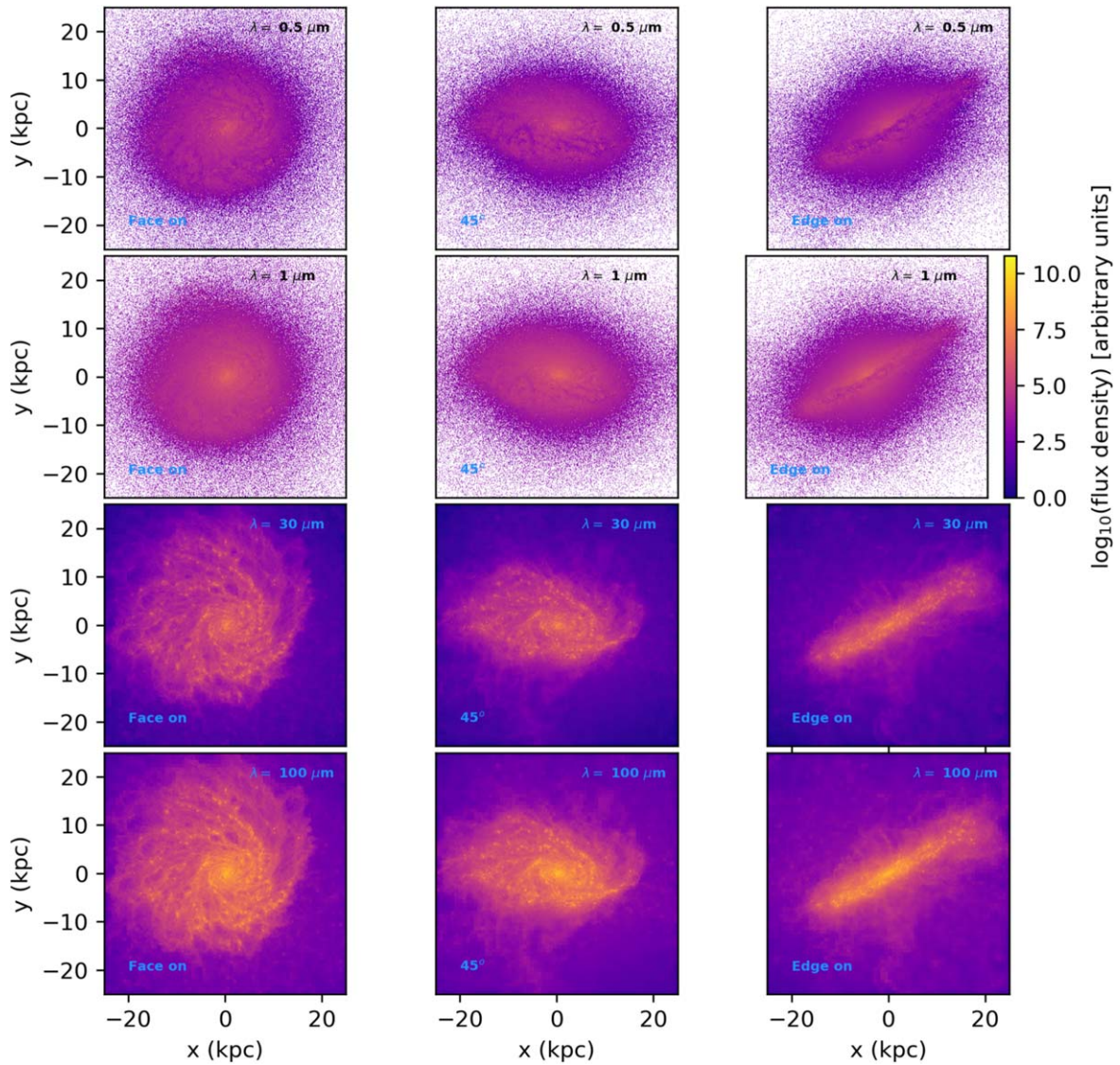


**Figure 9.** Example monochromatic images of model LATTE at  $\lambda = [0.5, 1, 30, 100] \mu\text{m}$  (rows) and at 3 different viewing angles (columns). As in Figure 8, the model galaxy is set at 30 Mpc.

POWDERDAY, as well as a verification of the code against prior results. Each of these could be a scientific investigation unto itself. We take a relatively shallow approach to each topic, deferring more thorough investigations to future work. We assumed the Padova stellar isochrones (Bertelli et al. 1994; Girardi et al. 2000; Marigo et al. 2008) and MILES spectral models (Sánchez-Blázquez et al. 2006) for each of these applications.

#### 4.1. Infrared SFR Tracers

The bolometric infrared luminosity is often used as a tracer of the total SFR of a galaxy, with the physical motivation that the ultraviolet radiation from young newly formed stars is likely to be absorbed and reprocessed by cold dust in the galaxy. Often-used literature calibrations (e.g., Kennicutt 1998; Murphy et al. 2011) are typically developed using population synthesis models with a relatively simplistic star formation history (or a stellar population modeled as a simple stellar population) alongside an assumed dust-covering fraction of the stellar population. Complications to these sorts of calibrations

include the contribution of older stellar populations to diffuse dust heating (and therefore adding additional infrared luminosity that does not originate from young, newly formed stars), as well as an AGN source term (Younger et al. 2009; Hopkins et al. 2010; Hayward et al. 2014; Narayanan et al. 2015).

As an example of the potential of POWDERDAY in investigating this issue, we compute the SEDs from the 1000 most massive galaxies in the redshift  $z = 2$  snapshot of the SIMBA M25N512 cosmological galaxy formation simulation. In the left panel of Figure 11, we compare the integrated infrared luminosity for this sample of galaxies (8–1000  $\mu\text{m}$  in the galaxy’s rest frame) to its 50 Myr averaged SFR. The solid blue line shows the Murphy et al. (2011) calibration between  $L_{\text{IR}}$  and the SFR (as reported by Kennicutt & Evans 2012).

At sufficiently low SFRs, the modeled galaxies diverge from the Murphy et al. (2011) relation due to a lack of sufficient dust obscuration of luminous sources (this is demonstrated via the color-coding of the points in the left panel of Figure 11, which denotes the galaxy angle-averaged  $A_V$ ). At SFRs  $\gtrsim 1 M_{\odot} \text{ yr}^{-1}$ , however, the dust obscuration rises sufficiently that the bolometric infrared luminosity serves as a reasonable tracer



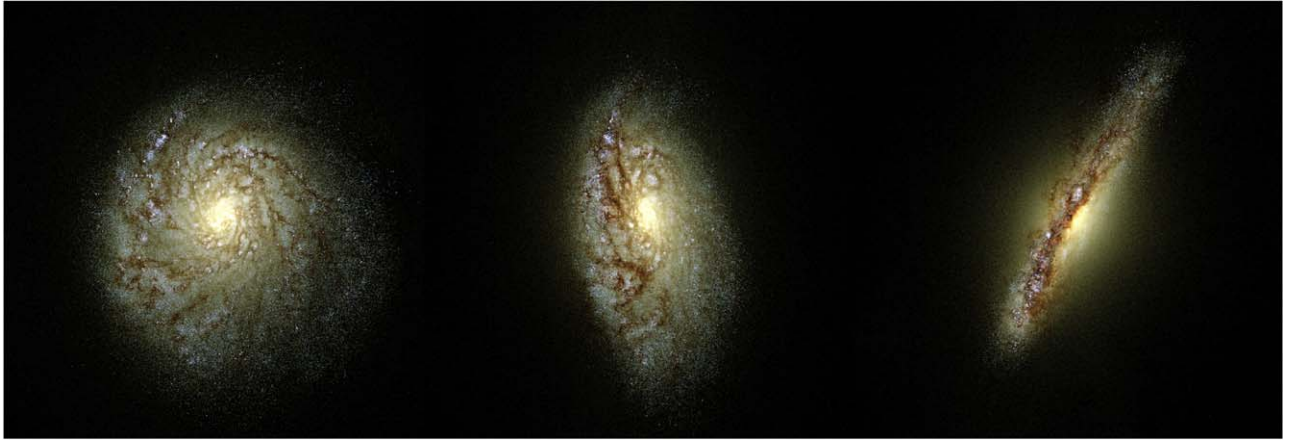


**Figure 10.** RGB images corresponding to 0.3, 0.5, and 1  $\mu\text{m}$  colors from model LATTE for three different viewing angles. Dust lanes in the galaxy (here, the dust mass is tied to the metal mass as a model assumption) are visible. As in Figure 8, the model galaxy is set at 30 Mpc. Images generated following the Lupton et al. (2004) scalings.

of the SFR based on empirical calibrations. At the highest luminosities modeled here ( $\sim 10^{11} L_{\odot}$ ), there is some tendency for the infrared luminosity to overestimate the SFR by a factor  $\sim 2$ , owing to the contribution of old stars. This effect is relatively small given the limited maximum SFRs in this small SIMBA box. Narayanan et al. (2015) demonstrated via cosmological zoom simulations of massive galaxies that factors of  $\sim 3$ – $4$  increase in the infrared luminosity from old stars can be possible in the most extreme (i.e.,  $\text{SFR} \sim 1000 M_{\odot} \text{yr}^{-1}$ ) cases.

In the right panel of Figure 11, we examine the impact of including an AGN as a radiating source. For this example, we assume that the black hole SED follows a Hopkins et al. (2007) spectrum and that the luminosity of the black hole is  $L = \eta \dot{M} c^2$ , where the efficiency  $\eta = 0.1$ . The blue shaded region shows a histogram of the observed infrared luminosity compared to what is expected given the galaxy SFR and the Murphy et al. (2011)  $\text{SFR}-L_{\text{IR}}$  calibration for the same 1000 galaxies as in the left panel of Figure 11. The salmon shaded region shows the same histogram for the same galaxies, but including AGN. As is clear, there is significantly more power toward large infrared luminosities, reflecting the impact of the AGN on the increased  $L_{\text{IR}}$  and the potential for overestimating the inferred SFR.

#### 4.2. Circumstellar AGB Dust in Low-metallicity Galaxies

One of the more powerful aspects of POWDERDAY is its generation of stellar SEDs on the fly (as opposed to via lookup tables). While this represents a fairly significant computational expense compared to utilizing lookup tables for the stellar SEDs, the trade-off is flexibility in being able to explore the impact of stellar physics on the emergent SED from galaxies.

To demonstrate an example of this, in Figure 12, we show the impact of including one such aspect of the underlying stellar model: the effect of circumstellar dust around AGB stars. Villaume et al. (2015) developed DUSTY radiative transfer models (Ivezic & Elitzur 1997; Ivezic et al. 1999) for AGB-phase stars that couple directly with the FSPS population synthesis code. As a result, this is trivially implementable in the POWDERDAY framework. In the left panel of Figure 12, we show the SED for an arbitrarily selected galaxy (galaxy 1) with a relatively low  $M_{\text{dust}}/M_{*}$  ratio from the SIMBA M25N512 cosmological simulation. As is clear, AGB dust can have a

significant impact on the mid-IR SEDs of galaxies with a relatively low dust content.

As has been discussed in previous works (e.g., Silva et al. 1998; Villaume et al. 2015), the impact of AGB dust on the mid-IR SED is dependent on the amount of diffuse dust in a galaxy. As the diffuse dust content increases, this takes over the contribution of circumstellar dust surrounding AGB stars in the mid-IR. To show this, we have modeled the SEDs from the top 1000 most massive galaxies from the redshift  $z = [0, 1, 2]$  snapshots from the SIMBA M25N512 cosmological simulation both with and without the contribution of circumstellar AGB dust. To simplify the analysis, we have not included our model for PAH emission (see Section 2.9). In the right panel of Figure 12, we plot the ratio of the 24  $\mu\text{m}$  (to serve as an arbitrary mid-IR wavelength) flux density for a model with AGB dust turned on to a model without AGB dust turned on as a function of the fractional dust mass in the galaxy. At low fractional dust content ( $M_{\text{dust}}/M_{*} \ll 1$ ), the fractional contribution of the circumstellar dust dominates in the mid-IR. As the diffuse dust content of the galaxy increases, however, the relative contribution of AGB dust decreases, and the ratio of the 24  $\mu\text{m}$  flux density for galaxies modeled with and without AGB dust converges to unity.

#### 4.3. Inclination-dependent Dust Attenuation Laws

The attenuation curve of a galaxy represents the effective amount of light lost from a source (typically, understood to mean stellar light) and is a fundamental quantity of interest in SED fitting (see Salim & Narayanan 2020, for a recent review of attenuation laws in galaxies). The attenuation curve reflects both extinction along the line of sight (due to absorption and scattering), as well as the contributions by both light scattered back into the line of sight and unobscured stars. It is therefore highly dependent on the intricacies of the star–dust geometry in a particular system, as well as the viewing angle. The dust attenuation law on galaxy-wide scales has been the subject of a number of theoretical investigations in recent years, in large part due to advances in coupling hydrodynamic galaxy simulations with dust radiative transfer packages (including POWDERDAY Jonsson 2006; Seon & Draine 2016; Narayanan et al. 2018a; Trayford et al. 2020).

In Figure 13, we investigate the role of galaxy inclination on the attenuation law. For this, we employ the LATTE simulation,

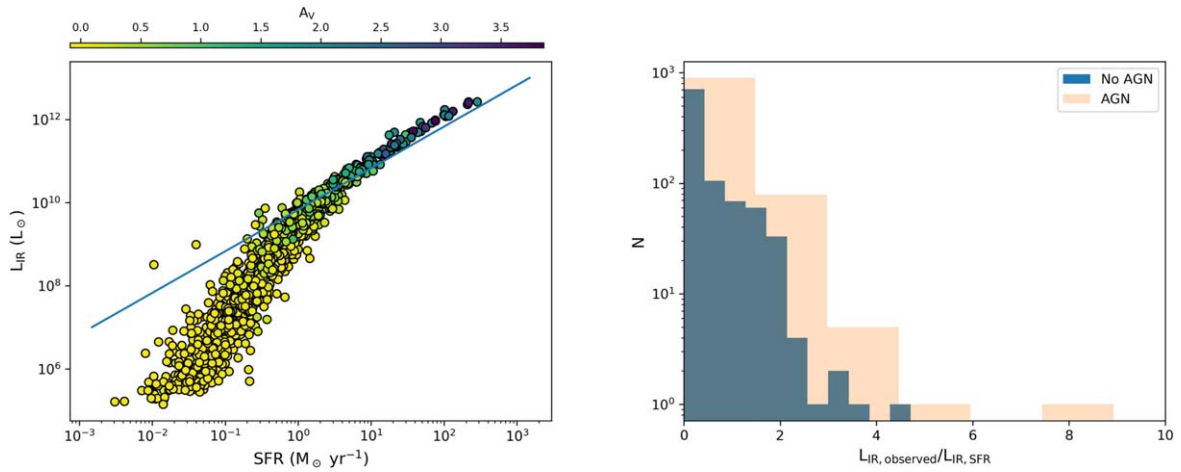


**Figure 11.** Left: infrared luminosity (integrated between 8 and  $1000\ \mu\text{m}$ ) vs. star formation rate for the 1000 most massive galaxies at redshift  $z = 2$  in the SIMBA M25N512 cosmological simulation. The solid line shows the Murphy et al. (2011) SFR– $L_{\text{IR}}$  relation as compiled in Kennicutt & Evans (2012). Below SFRs  $\lesssim 1\ M_{\odot}\ \text{yr}^{-1}$ , a lack of dust in galaxies drives a precipitous drop in the infrared luminosity with respect to SFR. Right: the impact of an AGN on the  $L_{\text{IR}}$ –SFR relationship in galaxies. Histograms show the ratio of the synthetic “observed” infrared luminosity to what one would expect from the Murphy et al. (2011) relationship, given the model galaxy’s SFR. As is clear, the AGN drives excess power toward high luminosities, which may result in overestimates of the SFR using a canonical  $L_{\text{IR}}$ –SFR relation for some galaxies.

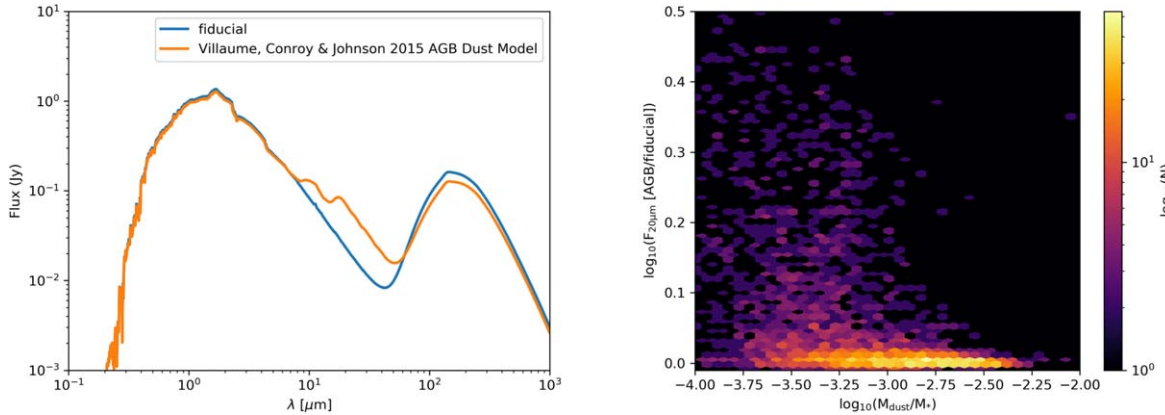


**Figure 12.** Impact of circumstellar AGB dust on the mid-IR SEDs of galaxies as a demonstration of the impact of stellar physics on POWDERDAY radiative transfer models. Left: example SEDs (without PAH models) of a quiescent galaxy with a low dust mass fraction from the SIMBA M25N512 simulation both including (orange) and not including (blue) the Villaume et al. (2015) model for circumstellar AGB dust. As is evident, in this galaxy with relatively low diffuse dust, the mid-IR flux is dominated by circumstellar AGB dust. Right: generalization of the left plot for 3000 galaxies at  $z = [0, 1, 2]$  from the same SIMBA M25N512 model, where we show the ratio of the  $24\ \mu\text{m}$  flux density (as a proxy for the mid-IR) for a model with and without AGB dust vs. the fractional dust content of the galaxy. Colored points show a heat map of individual galaxy snapshots, with the color bar on the right. When the diffuse dust content is sufficiently large, the flux in the mid-IR is dominated by diffuse dust, and the ratio of mid-IR flux for both models converges to 1.

as it has a clear disk-like morphology at its final redshift of  $z = 0$ , thus facilitating analysis. We calculate the attenuation law over 9 isotropic viewing angles. While we plot all viewing angles (in light gray), we highlight three particular angles in color that correspond to face-on, edge-on, and an intermediate angle, and show their corresponding  $30\ \mu\text{m}$  images. The attenuation curves are normalized at  $3000\ \text{\AA}$  to highlight changes in the slope of the law.

As is clear, there is a diverse range of ultraviolet slopes for the differing viewing angles of the model galaxy LATTE. As discussed in detail in the Salim & Narayanan (2020) review, these sorts of slope variations are typically ascribed to variations in the star–dust geometry between galaxies. To our knowledge, this is the first demonstration from a galaxy formed in a cosmological hydrodynamic simulation that slope changes in the attenuation curve can also be ascribed to the viewing angle of the galaxy: more edge-on views have larger differential attenuation in the UV than face-on views. This

point is amplified by the recent observational surveys of Salim et al. (2018) and Battisti et al. (2017), as well as the idealized models presented in Tuffs et al. (2004), Pierini et al. (2004), and Natale et al. (2015).

## 5. Discussion

### 5.1. Is 3D Dust Radiative Transfer Really Necessary?

We now ask the simple question: is dust radiative transfer actually necessary to capture the intricacies of the SEDs from galaxies? To quantify this, we compare the results of POWDERDAY dust radiative transfer modeling of galaxies (necessarily in three-dimensions) to simplified screen models, akin to what is traditionally used in SED fitting, or generating mock SEDs of galaxies from population synthesis modeling.

To develop this comparison, we have run POWDERDAY on the top 1000 most massive galaxies in the  $z = 0$  snapshot of the SIMBA M25N512 cosmological simulation. We then extract the

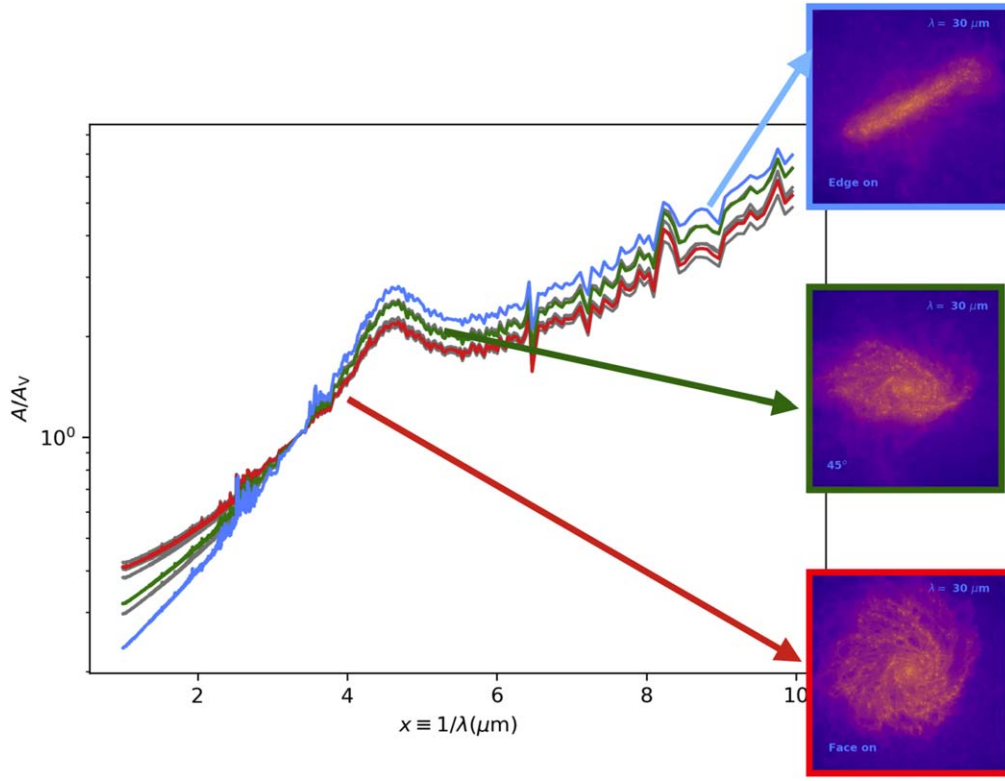


**Figure 13.** Impact of galaxy inclination angle on attenuation laws. Curves represent UV-NIR attenuation curves for model galaxy LATTE for nine viewing angles, with three particular angles highlighted in color that correspond to the images on the right (face on, edge on, and intermediary). Edge-on inclination angles display steeper normalized curves, while face-on views result in grayer (flatter) attenuation curves.

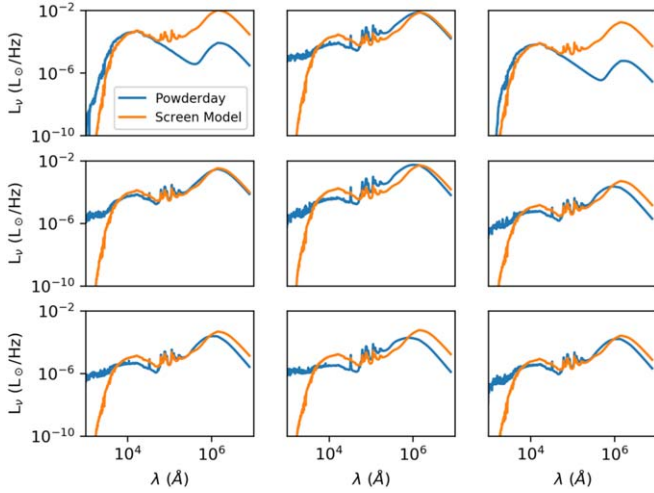


**Figure 14.** Comparison of 3D dust radiative transfer models of nine randomly selected galaxies in the SIMBA M25N512 cosmological simulation (at  $z = 0$ ; blue) compared against 1D dust screen models (orange). By and large, screen models do not capture the complexities of the star–dust ISM as 3D models do, and therefore overattenuate the UV and optical radiation.

star formation histories and metal enrichment histories of these galaxies at relatively high time resolution ( $\sim 150$  evenly spaced time bins over a Hubble time) and use those as inputs in FSPS to build a composite stellar population. Using the methods built into FSPS, we then place this composite stellar population behind a dust screen with Draine & Li (2007) dust properties. For this model, we fix the variable parameters in the

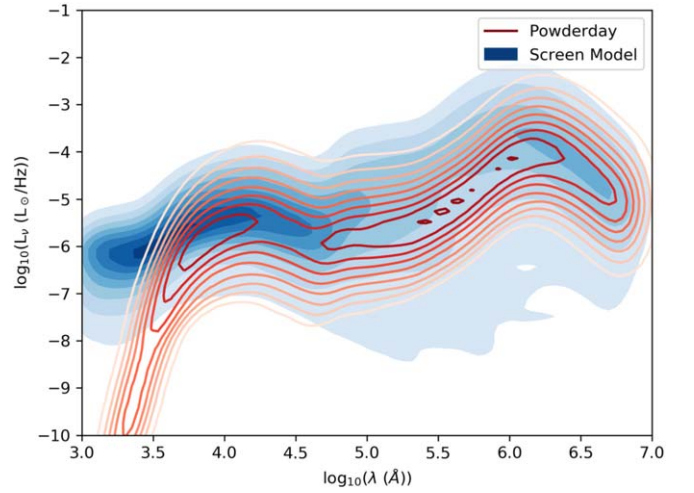


**Figure 15.** Same as Figure 14, though showing the results from the top 1000 most massive galaxies in the SIMBA M25N512 cosmological simulation at  $z = 0$ . Blue shows the POWDERDAY 3D dust radiative transfer models compared against 1D dust screen models (red). The colors/contours show the density of the number of models with a given SED shape.

Draine & Li (2007) model to their defaults ( $U_{\min} = 0.1$ ,  $q_{\text{PAH}} = 3.5$  and  $\gamma = 0.01$ ), noting that some modern SED fitting software packages have the ability to vary these parameters when modeling infrared SEDs (e.g., Leja et al. 2017, 2019; Johnson 2019; Johnson et al. 2019).

We show the results of these mock SED models in Figure 14, which shows the SEDs of a random selection of



nine galaxies. In Figure 15, we show the results from all of the modeled galaxies as a density plot. There are fairly substantial differences in the modeled UV-optical SED. The traditional screen model effectively treats all of the stars in the galaxy as a single source and all of the dust as a single site of obscuration. By ignoring the complex mixing of gas and dust in galaxies, and the consequent impact on the effective optical depths (e.g., Narayanan et al. 2018a, 2018b), the simplified screen model tends to overattenuate the UV and optical regime of the SED. Conversely, the 3D dust radiative transfer modeling exhibits significantly more leakage in the UV, an effect that can impact the dust attenuation curve (Salim & Narayanan 2020), as well as manifestations in related relations such as the  $\text{IRX}-\beta$  relation in galaxies (Popping et al. 2017a).

### 5.2. Future Directions and Current Limitations

While POWDERDAY is an extremely flexible dust radiative transfer package that contains a number of state-of-the-art algorithms (thanks to the continued development of the software that it bundles), there are a number of future code development directions that would be valuable.

A natural direction forward would be to include models for molecular and atomic line emission from neutral and molecular gas. Simulations with software such as DESPOTIC (Krumholz 2013) that model emission from photodissociation regions and molecular gas have demonstrated that line emission from these regions typically depends on (alongside the physical properties of the gas itself, which is typically returned from a given hydrodynamic galaxy simulation) the cosmic-ray flux and the incident UV radiation field (e.g., Narayanan & Krumholz 2017; Li et al. 2018). Generally, simulations of line emission from galaxy simulations have had to employ local approximations for the latter quantity (Olsen et al. 2015, 2017; Leung et al. 2020, see also Olsen et al. 2018 for a review of some of these issues), ignoring the impact of diffuse dust on large scales. This quantity can, in principle, be derived explicitly from dust radiative transfer modeling. A valuable addition would therefore be to incorporate this information in modeling the atomic and molecular line emission from galaxy formation simulations.

In the future, we additionally envision POWDERDAY taking advantage of modern algorithm developments in the modeling of dust in galaxy formation simulations. As we discussed in Section 2.8, POWDERDAY can already include models for spatially varying dust content that derives directly from hydrodynamic simulations (e.g., McKinnon et al. 2016; Li et al. 2019). However, newer approaches are now allowing for the evolution of the size distribution of grains that vary spatially across the galaxy (Hirashita 2015; Aoyama et al. 2018; McKinnon et al. 2018; Hou et al. 2019; Q Li et al. 2021, in preparation). When coupling these size distributions with an assumed extinction efficiency, these spatially varying size distributions can be used to model the dust extinction law. A major step forward for dust radiative transfer codes will be to allow for the ability to include nonuniform extinction laws as returned from models such as these, in order to develop ever-more realistic SED models from galaxies. By coupling with simulations that include a computed size distribution of dust grains, this will allow POWDERDAY to move beyond our current (non-self-consistent) setup of including PAHs via a user-set fraction of ultra-small, very small, and big dust grains. Of course, a realistic treatment of PAH emission will depend

on the inclusion of stochastic heating of dust grains, which our model currently does not include (e.g., Draine & Li 2001).

Finally, an important direction in adding realism to our nebular line emission models will be to take advantage of the results from models of ionized gas surrounding massive stars that fully solve the equations of motion for spherical ionized shells in the face of a diverse set of physics, such as stellar winds, supernova energy, radiation pressure, and gravity (e.g., Dopita et al. 2005; Pellegrini et al. 2020a, 2020b). Dynamical H II region models such as these can be used to set the size/inner radius of H II regions, adding significant realism to the line-emission modeling.

## 6. Summary

We have presented the first release of the POWDERDAY dust radiative transfer package, which is designed to extract synthetic broadband SEDs and nebular line emission from hydrodynamic idealized and cosmological galaxy formation simulations. POWDERDAY is designed with ease of use and flexibility in mind, aiming to eliminate interface hurdles between practitioners of different hydrodynamic galaxy formation methods and radiative transfer. In particular, some major features of POWDERDAY include the following:

1. POWDERDAY is designed with a high level of flexibility in mind. Users have the ability to vary many aspects of the stellar emission via the bindings to the flexible FSPS population synthesis code, nebular line emission from H II regions, and models for the dust content in galaxies.
2. We have implemented front ends in POWDERDAY to seamlessly interface with a number of hydrodynamic galaxy formation packages (through the use of YT as an intermediary), including GIZMO, AREPO, GASOLINE, CHANGA and ENZO.
3. By leveraging HYPERION as our dust radiative transfer solver, we are able to maintain a high level of scalability and perform the radiative transfer over octree, adaptive, and Voronoi meshes.
4. We include multiple models for optional emission from AGNs.





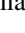






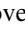



We have additionally demonstrated the capabilities of POWDERDAY via a number of scientific applications:

1. We have examined the relationship between the SFR and infrared luminosity (8–1000  $\mu\text{m}$ ) in a sample of cosmologically simulated galaxies. While the bulk of the galaxies fall on the Murphy et al. (2011) relationship between  $L_{\text{IR}}$  and SFR, galaxies at very low SFRs deviate significantly owing to a lack of dust. At the high-SFR end, the implied SFR from the  $L_{\text{IR}}$  can exceed the true SFR due to both a contribution of older stars to the heating of diffuse dust, as well as (when present) contribution from AGNs (Figure 11).
2. We have modeled the contribution of circumstellar AGB dust to the mid-infrared flux of galaxies using the Villaume et al. (2015) model for AGB dust emission. For quiescent galaxies with a relatively low dust content, circumstellar AGB emission can provide a significant boost to the mid-IR flux. As the  $M_{\text{dust}}/M_*$  ratio increases, however, the impact of AGB dust emission becomes negligible (Figure 12).

3. We investigated the role of inclination angle on the integrated dust attenuation law from a model disk galaxy. Edge-on views of the galaxy tend to show steeper attenuation laws in the ultraviolet, while face-on views result in grayer (flatter) curves.
4. We have compared the results from 3D dust radiative transfer to simplified screen models (Figure 15). Generally, full 3D radiative transfer shows more power at UV and optical wavelengths (and consequently, less in the infrared) due to a more complex star–dust geometry than screen models typically allow for.

In the course of developing POWDERDAY, numerous individuals have provided substantial help. First and foremost, we are eternally grateful to the hundreds of members of the YT community both for their contributions to the YT codebase as well as for their participation and positive-natured support in the YT email lists and Slack page. Without this inclusive community, POWDERDAY would have never been possible. We thank Nell Byler, Romeel Davé, Ross Fadely, Kevin Flaherty, Nathan Goldbaum, Fabio Governato, Chris Hayward, Cameron Hummels, Ben Keller, Dusan Keres, Patrick Sheehan, Rachel Somerville, Brian Svoboda, and Greg Walth for helpful conversations along the way. We are grateful to Oscar Agertz, Mike Butler, Ji-hoon Kim, Keita Todoroki, Kentaro Nagamine, and James Wadsley for their willingness to share sample AGORA snapshots in advance of their publication (which enabled early POWDERDAY testing), and Mike Tremmel, Nicole Sanchez, Andrew Pontzen, Paul Torrey, and Federico Marinacci for sharing CHANGA and AREPO SMUGGLE sample outputs for testing. We thank the countless scientists who have beta tested POWDERDAY over the years, including Hollis Akins, David Ball, Derrick Carr, Charlotte Christensen, Joel Christian, Jarren Jennings, Katarina Kraljic, Reilly Millburn, Emily Moser, Justin Otter, Gergo Popping, Spencer Scott, Emery Trott, and David Zegeye. D.N. thanks Vicente Rodriguez-Gomez, Paul Torrey, Federico Marinacci, and Laura Blecha for their assistance in working with AREPO simulation outputs. We thank the FIRE-2 collaboration for their having made the LATTE simulation results public. We are grateful to Maarten Baes and Peter Camps for their assistance in developing the SKIRT comparison with POWDERDAY. D.N. additionally expresses deep appreciation toward Joe Cammisa at Haverford College and the UF Research Computing group for their roles in maintaining the Fock and HiPerGator high-performance computing clusters, respectively, where the main development of POWDERDAY took place. Partial support for DN was provided by NSF grants AST-1009452, AST-1442650, and NASA HST AR-13906.001 from the Space Telescope Science Institute, which is operated by the Association of Universities for Research in Astronomy, Incorporated, under NASA contract NAS5-26555, and a Cottrell College Science Award awarded by the Research Corporation for Science Advancement. A.J.K. acknowledges an STFC studentship grant ST/S505365/1. J.H.W. is supported by NSF grants AST-1614333 and OAC-1835213 and NASA grants NNX17AG23G and 80NSSC20K0520. M.J.T. was supported in part by the Gordon and Betty Moore Foundation’s Data-Driven Discovery Initiative through Grant GBMF4561. Finally, D.N. expresses deep appreciation for the Aspen Center for Physics, at which the idea for (and naming of, on a bluebird day at Ajax Mountain) POWDERDAY came about.

## ORCID iDs

Desika Narayanan  <https://orcid.org/0000-0002-7064-4309>  
 Matthew J. Turk  <https://orcid.org/0000-0002-5294-0198>  
 Thomas Robitaille  <https://orcid.org/0000-0002-8642-1329>  
 Ashley J. Kelly  <https://orcid.org/0000-0003-3850-4469>  
 B. Connor McClellan  <https://orcid.org/0000-0002-6040-8281>  
 Ray S Sharma  <https://orcid.org/0000-0001-8350-4535>  
 Ena Choi  <https://orcid.org/0000-0002-8131-6378>  
 Charlie Conroy  <https://orcid.org/0000-0002-1590-8551>  
 Benjamin D. Johnson  <https://orcid.org/0000-0002-9280-7594>  
 Benjamin Kimock  <https://orcid.org/0000-0002-3160-7679>  
 Christopher C. Lovell  <https://orcid.org/0000-0001-7964-5933>  
 Sidney Lower  <https://orcid.org/0000-0003-4422-8595>  
 George C. Privon  <https://orcid.org/0000-0003-3474-1125>  
 Gregory F. Snyder  <https://orcid.org/0000-0002-4226-304X>  
 John H. Wise  <https://orcid.org/0000-0003-1173-8847>

## References

- Abruzzo, M. W., Narayanan, D., Davé, R., & Thompson, R. 2018, arXiv:1803.02374
- Alonso-Herrero, A., Quillen, A. C., Rieke, G. H., Ivanov, V. D., & Efstathiou, A. 2003, *AJ*, **126**, 81
- Aoyama, S., Hou, K.-C., Hirashita, H., Nagamine, K., & Shimizu, I. 2018, *MNRAS*, **478**, 4905
- Aoyama, S., Hou, K.-C., Shimizu, I., et al. 2017, *MNRAS*, **466**, 105
- Asano, R. S., Takeuchi, T. T., Hirashita, H., & Inoue, A. K. 2013, *EP&S*, **65**, 213
- Astropy Collaboration, Robitaille, T. P., Tollerud, E. J., et al. 2013, *A&A*, **558**, A33
- Baes, M., & Camps, P. 2015, *A&C*, **12**, 33
- Baes, M., Trčka, A., Camps, P., et al. 2019, *MNRAS*, **484**, 4069
- Baes, M., Trčka, A., Camps, P., et al. 2020, *MNRAS*, **494**, 2912
- Baes, M., Verstappen, J., De Looze, I., et al. 2011, *ApJS*, **196**, 22
- Battisti, A. J., Calzetti, D., & Chary, R. R. 2017, *ApJ*, **851**, 90
- Baugh, C. M., Lacey, C. G., Frenk, C. S., et al. 2005, *MNRAS*, **356**, 1191
- Benson, A. J. 2010, *PhR*, **495**, 33
- Bertelli, G., Bressan, A., Chiosi, C., Fagotto, F., & Nasi, E. 1994, *A&AS*, **106**, 275
- Blain, A. W., Smail, I., Ivison, R. J., et al. 2002, *PhR*, **369**, 111
- Blanton, M. R., & Moustakas, J. 2009, *ARA&A*, **47**, 159
- Blecha, L., Snyder, G. F., Satyapal, S., & Ellison, S. L. 2018, *MNRAS*, **478**, 3056
- Bolatto, A. D., Wolfire, M., & Leroy, A. K. 2013, *ARA&A*, **51**, 207
- Brummel-Smith, C., Bryan, G., Butsky, I., et al. 2019, *JOSS*, **4**, 1636
- Bryan, G. L., Norman, M. L., O’Shea, B. W., et al. 2014, *ApJS*, **211**, 19
- Byler, N., Dalcanton, J. J., Conroy, C., et al. 2018, *ApJ*, **863**, 14
- Byler, N., Dalcanton, J. J., Conroy, C., et al. 2019, *AJ*, **158**, 2
- Byler, N., Dalcanton, J. J., Conroy, C., & Johnson, B. D. 2017, *ApJ*, **840**, 44
- Camps, P., & Baes, M. 2015, *A&C*, **9**, 20
- Camps, P., & Baes, M. 2020, *A&C*, **31**, 100381
- Camps, P., Trčka, A., Trayford, J., et al. 2018, *ApJS*, **234**, 20
- Carilli, C. L., & Walter, F. 2013, *ARA&A*, **51**, 105
- Casey, C. M. 2012, *MNRAS*, **425**, 3094
- Casey, C. M., Narayanan, D., & Cooray, A. 2014, *PhR*, **541**, 45
- Cen, R., & Kimm, T. 2014, *ApJ*, **782**, 32
- Chabrier, G. 2003, *PASP*, **115**, 763
- Chakrabarti, S., Cox, T. J., Hernquist, L., et al. 2007, *ApJ*, **658**, 840
- Chakrabarti, S., Fenner, Y., Cox, T. J., Hernquist, L., & Whitney, B. A. 2008, *ApJ*, **688**, 972
- Chakrabarti, S., & Whitney, B. A. 2009, *ApJ*, **690**, 1432
- Chandar, R., Whitmore, B. C., Calzetti, D., & O’Connell, R. 2014, *ApJ*, **787**, 17
- Chandar, R., Whitmore, B. C., Dinino, D., et al. 2016, *ApJ*, **824**, 71
- Cochrane, R. K., Hayward, C. C., Anglés-Alcázar, D., et al. 2019, *MNRAS*, **488**, 1779
- Conroy, C. 2013, *ARA&A*, **51**, 393
- Conroy, C., & Gunn, J. E. 2010, *ApJ*, **712**, 833

- Conroy, C., Gunn, J. E., & White, M. 2009, *ApJ*, **699**, 486
- Conroy, C., White, M., & Gunn, J. E. 2010, *ApJ*, **708**, 58
- Cowley, W. I., Lacey, C. G., Baugh, C. M., et al. 2019, *MNRAS*, **487**, 3082
- Cowley, W. I., Lacey, C. G., Baugh, C. M., & Cole, S. 2015, *MNRAS*, **446**, 1784
- Daddi, E., Cimatti, A., Renzini, A., et al. 2004, *ApJ*, **617**, 746
- Dalcanton, J. J., Williams, B. F., Lang, D., et al. 2012, *ApJS*, **200**, 18
- Davé, R., Anglés-Alcázar, D., Narayanan, D., et al. 2019, *MNRAS*, **486**, 2827
- Davé, R., Finlator, K., & Oppenheimer, B. D. 2012, *MNRAS*, **421**, 98
- Davé, R., Katz, N., Oppenheimer, B. D., Kollmeier, J. A., & Weinberg, D. H. 2013, *MNRAS*, **434**, 2645
- Davé, R., Thompson, R., & Hopkins, P. F. 2016, *MNRAS*, **462**, 3265
- De Looze, I., Fritz, J., Baes, M., et al. 2014, *A&A*, **571**, A69
- De Vis, P., Jones, A., Viaene, S., et al. 2019, *A&A*, **623**, A5
- Domínguez-Tenreiro, R., Obreja, A., Granato, G. L., et al. 2014, *MNRAS*, **439**, 3868
- Dopita, M. A., Groves, B. A., Fischera, J., et al. 2005, *ApJ*, **619**, 755
- Draine, B. T. 2003, *ARA&A*, **41**, 241
- Draine, B. T., & Li, A. 2001, *ApJ*, **551**, 807
- Draine, B. T., & Li, A. 2007, *ApJ*, **657**, 810
- Dullemond, C. P., Juhasz, A., Pohl, A., et al. 2012, RADMC-3D: A Multi-purpose Radiative Transfer Tool, Astrophysics Source Code Library, ascl:1202.015
- Dunlop, J. S. 2011, in ASP Conf. Ser. 446, Galaxy Evolution: Infrared to Millimeter Wavelength Perspective, ed. W. Wang et al. (San Francisco, CA: ASP), **209**
- Dwek, E. 1998, *ApJ*, **501**, 643
- Efstathiou, A., Rowan-Robinson, M., & Siebenmorgen, R. 2000, *MNRAS*, **313**, 734
- Feldmann, R., Gnedin, N. Y., & Kravtsov, A. V. 2011, *ApJ*, **732**, 115
- Ferland, G. J., Porter, R. L., van Hoof, P. A. M., et al. 2013, *RMxAA*, **49**, 137
- Finkelstein, S. L. 2016, *PASA*, **33**, e037
- Finkelstein, S. L., Papovich, C., Dickinson, M., et al. 2013, *Natur*, **502**, 524
- Finkelstein, S. L., Song, M., Behroozi, P., et al. 2015, *ApJ*, **814**, 95
- Gadotti, D. A., Baes, M., & Falony, S. 2010, *MNRAS*, **403**, 2053
- Girardi, L., Bressan, A., Bertelli, G., & Chiosi, C. 2000, *A&AS*, **141**, 371
- Gjergo, E., Granato, G. L., Murante, G., et al. 2018, *MNRAS*, **479**, 2588
- Gordon, K. D., Misselt, K. A., Witt, A. N., & Clayton, G. C. 2001, *ApJ*, **551**, 269
- Granato, G. L., Lacey, C. G., Silva, L., et al. 2000, *ApJ*, **542**, 710
- Granato, G. L., Ragone-Figueroa, C., Domínguez-Tenreiro, R., et al. 2015, *MNRAS*, **450**, 1320
- Hayward, C. C., Kereš, D., Jonsson, P., et al. 2011, *ApJ*, **743**, 159
- Hayward, C. C., Lanz, L., Ashby, M. L. N., et al. 2014, *MNRAS*, **445**, 1598
- Hayward, C. C., Narayanan, D., Kereš, D., et al. 2013, *MNRAS*, **428**, 2529
- Hickox, R. C., Mullaney, J. R., Alexander, D. M., et al. 2014, *ApJ*, **782**, 9
- Hirashita, H. 2015, *MNRAS*, **447**, 2937
- Hirashita, H., & Aoyama, S. 2019, *MNRAS*, **482**, 2555
- Hodge, J. A., & da Cunha, E. 2020, arXiv:2004.00934
- Hopkins, P. F. 2014, GIZMO: Multi-method Magneto-hydrodynamics + Gravity Code, Astrophysics Source Code Library, ascl:1410.003
- Hopkins, P. F. 2015, *MNRAS*, **450**, 53
- Hopkins, P. F. 2017, arXiv:1712.01294
- Hopkins, P. F., & Hernquist, L. 2009, *ApJ*, **698**, 1550
- Hopkins, P. F., Narayanan, D., & Murray, N. 2013, *MNRAS*, **432**, 2647
- Hopkins, P. F., Richards, G. T., & Hernquist, L. 2007, *ApJ*, **654**, 731
- Hopkins, P. F., Wetzel, A., Kereš, D., et al. 2018, *MNRAS*, **480**, 800
- Hopkins, P. F., Younger, J. D., Hayward, C. C., Narayanan, D., & Hernquist, L. 2010, *MNRAS*, **402**, 1693
- Hou, K.-C., Aoyama, S., Hirashita, H., Nagamine, K., & Shimizu, I. 2019, *MNRAS*, **485**, 1727
- Hou, K.-C., Hirashita, H., Nagamine, K., Aoyama, S., & Shimizu, I. 2017, *MNRAS*, **469**, 870
- Ivezic, Z., & Elitzur, M. 1997, *MNRAS*, **287**, 799
- Ivezic, Z., Nenkova, M., & Elitzur, M. 1999, DUSTY: Radiation Transport in a Dusty Environment, Astrophysics Source Code Library, ascl:9911.001
- Johnson, B. D. 2019, SEDPY: Modules for Storing and Operating on Astronomical Source Spectral Energy Distribution, Astrophysics Source Code Library, ascl:1905.026
- Johnson, B. D., Leja, J. L., Conroy, C., & Speagle, J. S. 2019, Prospector: Stellar Population Inference from Spectra and SEDs, Astrophysics Source Code Library, ascl:1905.025
- Jonsson, P. 2006, *MNRAS*, **372**, 2
- Jonsson, P., Groves, B. A., & Cox, T. J. 2010, *MNRAS*, **403**, 17
- Jonsson, P., & Primack, J. R. 2010, *NewA*, **15**, 509
- Katsianis, A., Gonzalez, V., Barrientos, D., et al. 2020, *MNRAS*, **492**, 5592
- Kauffmann, G., & Heckman, T. M. 2009, *MNRAS*, **397**, 135
- Kennicutt, R. C., Calzetti, D., Aniano, G., et al. 2011, *PASP*, **123**, 1347
- Kennicutt, R. C., & Evans, N. J. 2012, *ARA&A*, **50**, 531
- Kennicutt, R. C., Jr. 1998, *ARA&A*, **36**, 189
- Kennicutt, R. C., Jr., Armus, L., Bendo, G., et al. 2003, *PASP*, **115**, 928
- Kim, J.-h., Abel, T., Agertz, O., et al. 2014, *ApJS*, **210**, 14
- Kim, J.-h., Agertz, O., Teyssier, R., et al. 2016, *ApJ*, **833**, 202
- Kroupa, P. 2002, *Sci*, **295**, 82
- Kroupa, P., Tout, C. A., & Gilmore, G. 1993, *MNRAS*, **262**, 545
- Krumholz, M. R. 2013, *MNRAS*, **437**, 1622
- Kulier, A., Galaz, G., Padilla, N. D., & Trayford, J. W. 2019, arXiv:1910.05345
- Law, D. R., Shapley, A. E., Steidel, C. C., et al. 2012, *Natur*, **487**, 338
- Leja, J., Carnall, A. C., Johnson, B. D., Conroy, C., & Speagle, J. S. 2019, *ApJ*, **876**, 3
- Leja, J., Johnson, B. D., Conroy, C., van Dokkum, P. G., & Byler, N. 2017, *ApJ*, **837**, 170
- Leung, T. K. D., Olsen, K. P., Somerville, R. S., et al. 2020, arXiv:2004.11912
- Li, Q., Narayanan, D., & Davé, R. 2019, *MNRAS*, **490**, 1425
- Li, Q., Narayanan, D., Davé, R., & Krumholz, M. R. 2018, *ApJ*, **869**, 73
- Li, Y., Gu, M. F., Yajima, H., Zhu, Q., & Maji, M. 2020, *MNRAS*, **494**, 1919
- Liang, L., Feldmann, R., Faucher-Giguère, C.-A., et al. 2018, *MNRAS*, **478**, L83
- Liang, L., Feldmann, R., Kereš, D., et al. 2019, *MNRAS*, **489**, 1397
- Lotz, J. M., Jonsson, P., Cox, T. J., & Primack, J. R. 2010a, *MNRAS*, **404**, 575
- Lotz, J. M., Jonsson, P., Cox, T. J., & Primack, J. R. 2010b, *MNRAS*, **404**, 590
- Lower, S., Narayanan, D., Leja, J., et al. 2020, arXiv:2006.03599
- Lucy, L. B. 1999, *A&A*, **344**, 282
- Lupton, R., Blanton, M. R., Fekete, G., et al. 2004, *PASP*, **116**, 133
- Lutz, D. 2014, *ARA&A*, **52**, 373
- Ma, X., Hayward, C. C., Casey, C. M., et al. 2019, *MNRAS*, **487**, 1844
- Madau, P., & Dickinson, M. 2014, *ARA&A*, **52**, 415
- Maraston, C., Daddi, E., Renzini, A., et al. 2006, *ApJ*, **652**, 85
- Marigo, P., Girardi, L., Bressan, A., et al. 2008, *A&A*, **482**, 883
- Marinacci, F., Sales, L. V., Vogelsberger, M., Torrey, P., & Springel, V. 2019, *MNRAS*, **489**, 4233
- Mason, R. E., Geballe, T. R., Packham, C., et al. 2006, *ApJ*, **640**, 612
- Mathis, J. S., Mezger, P. G., & Panagia, N. 1983, *A&A*, **500**, 259
- McAlpine, S., Smail, I., Bower, R. G., et al. 2019, *MNRAS*, **488**, 2440
- McKinnon, R., Torrey, P., & Vogelsberger, M. 2016, *MNRAS*, **457**, 3775
- McKinnon, R., Vogelsberger, M., Torrey, P., Marinacci, F., & Kannan, R. 2018, *MNRAS*, **478**, 2851
- Menon, H., Wesolowski, L., Zheng, G., et al. 2015, *ComAC*, **2**, 1
- Michałowski, M., Hjorth, J., & Watson, D. 2010, *A&A*, **514**, A67
- Misselt, K. A., Gordon, K. D., Clayton, G. C., & Wolff, M. J. 2001, *ApJ*, **551**, 277
- Murphy, E. J., Condon, J. J., Schinnerer, E., et al. 2011, *ApJ*, **737**, 67
- Naab, T., & Ostriker, J. P. 2017, *ARA&A*, **55**, 59
- Narayanan, D., Conroy, C., Davé, R., Johnson, B. D., & Popping, G. 2018a, *ApJ*, **869**, 70
- Narayanan, D., Cox, T. J., Hayward, C. C., & Hernquist, L. 2011a, *MNRAS*, **412**, 287
- Narayanan, D., Cox, T. J., Hayward, C. C., Younger, J. D., & Hernquist, L. 2009, *MNRAS*, **400**, 1919
- Narayanan, D., & Davé, R. 2012, *MNRAS*, **423**, 3601
- Narayanan, D., & Davé, R. 2013, *MNRAS*, **436**, 2892
- Narayanan, D., Davé, R., Johnson, B. D., et al. 2018b, *MNRAS*, **474**, 1718
- Narayanan, D., Dey, A., Hayward, C. C., et al. 2010b, *MNRAS*, **407**, 1701
- Narayanan, D., Hayward, C. C., Cox, T. J., et al. 2010a, *MNRAS*, **401**, 1613
- Narayanan, D., Krumholz, M., Ostriker, E. C., & Hernquist, L. 2011b, *MNRAS*, **418**, 664
- Narayanan, D., & Krumholz, M. R. 2017, *MNRAS*, **467**, 50
- Narayanan, D., Krumholz, M. R., Ostriker, E. C., & Hernquist, L. 2012, *MNRAS*, **421**, 3127
- Narayanan, D., Turk, M., Feldmann, R., et al. 2015, *Natur*, **525**, 496
- Natale, G., Popescu, C. C., Tuffs, R. J., et al. 2015, *MNRAS*, **449**, 243
- Natale, G., Popescu, C. C., Tuffs, R. J., & Semionov, D. 2014, *MNRAS*, **438**, 3137
- Nenkova, M., Sirocky, M. M., Ivezić, Ž., & Elitzur, M. 2008a, *ApJ*, **685**, 147
- Nenkova, M., Sirocky, M. M., Nikutta, R., Ivezić, Ž., & Elitzur, M. 2008b, *ApJ*, **685**, 160
- Novak, G. S., Ostriker, J. P., & Ciotti, L. 2011, *ApJ*, **737**, 26
- Nozawa, T., Asano, R. S., Hirashita, H., & Takeuchi, T. T. 2015, *MNRAS*, **447**, L16
- Oesch, P. A., Bouwens, R. J., Illingworth, G. D., Labbé, I., & Stefanon, M. 2018, *ApJ*, **855**, 105



- Oesch, P. A., van Dokkum, P. G., Illingworth, G. D., et al. 2015, *ApJL*, **804**, L30
- Olsen, K., Greve, T. R., Narayanan, D., et al. 2017, *ApJ*, **846**, 105
- Olsen, K. P., Greve, T. R., Narayanan, D., et al. 2015, *ApJ*, **814**, 76
- Olsen, K., Pallottini, A., Wofford, A., et al. 2018, *Galax*, **6**, 100
- Pastrav, B. A., Popescu, C. C., Tuffs, R. J., & Sansom, A. E. 2013, *A&A*, **557**, A137
- Pellegrini, E. W., Rahner, D., Reissl, S., et al. 2020a, *MNRAS*, **496**, 339
- Pellegrini, E. W., Reissl, S., Rahner, D., et al. 2020b, *MNRAS*, **498**, 3193
- Pierini, D., Gordon, K. D., Witt, A. N., & Madsen, G. J. 2004, *ApJ*, **617**, 1022
- Pietrinferni, A., Cassisi, S., Salaris, M., & Castelli, F. 2004, *ApJ*, **612**, 168
- Pillepich, A., Nelson, D., Hernquist, L., et al. 2018, *MNRAS*, **475**, 648
- Poncelet, A., Perrin, G., & Sol, H. 2006, *A&A*, **450**, 483
- Popping, G., Puglisi, A., & Norman, C. A. 2017a, *MNRAS*, **472**, 2315
- Popping, G., Somerville, R. S., & Galametz, M. 2017b, *MNRAS*, **471**, 3152
- Privon, G. C., Narayanan, D., & Davé, R. 2018, *ApJ*, **867**, 102
- Rémy-Ruyer, A., Madden, S. C., Galliano, F., et al. 2014, *A&A*, **563**, A31
- Richards, G. T., Lacy, M., Storrie-Lombardi, L. J., et al. 2006, *ApJS*, **166**, 470
- Robitaille, T. P. 2011, *A&A*, **536**, A79
- Robitaille, T. P., Churchwell, E., Benjamin, R. A., et al. 2012, *A&A*, **545**, A39
- Rodriguez-Gomez, V., Snyder, G. F., Lotz, J. M., et al. 2019, *MNRAS*, **483**, 4140
- Salim, S., Boquien, M., & Lee, J. C. 2018, *ApJ*, **859**, 11
- Salim, S., & Narayanan, D. 2020, arXiv:2001.03181
- Salpeter, E. E. 1955, *ApJ*, **121**, 161
- Sanchez, N. N., Werk, J. K., Tremmel, M., et al. 2019, *ApJ*, **882**, 8
- Sánchez-Blázquez, P., Peletier, R. F., Jiménez-Vicente, J., et al. 2006, *MNRAS*, **371**, 703
- Scannapieco, C., Gadotti, D. A., Jonsson, P., & White, S. D. M. 2010, *MNRAS*, **407**, L41
- Schaller, G., Schaerer, D., Meynet, G., & Maeder, A. 1992, *A&AS*, **96**, 269
- Schartmann, M., Meisenheimer, K., Camenzind, M., Wolf, S., & Henning, T. 2005, *A&A*, **437**, 861
- Schaye, J., Crain, R. A., Bower, R. G., et al. 2015, *MNRAS*, **446**, 521
- Scoville, N., Aussel, H., Sheth, K., et al. 2014, *ApJ*, **783**, 84
- Seon, K.-I., & Draine, B. T. 2016, *ApJ*, **833**, 201
- Shapley, A. E. 2011, *ARA&A*, **49**, 525
- Silva, L., Granato, G. L., Bressan, A., & Danese, L. 1998, *ApJ*, **509**, 103
- Snyder, G. F., Cox, T. J., Hayward, C. C., Hernquist, L., & Jonsson, P. 2011, *ApJ*, **741**, 77
- Snyder, G. F., Hayward, C. C., Sajina, A., et al. 2013, *ApJ*, **768**, 168
- Snyder, G. F., Lotz, J., Moody, C., et al. 2015a, *MNRAS*, **451**, 4290
- Snyder, G. F., Lotz, J. M., Rodriguez-Gomez, V., et al. 2017, *MNRAS*, **468**, 207
- Snyder, G. F., Rodriguez-Gomez, V., Lotz, J. M., et al. 2019, *MNRAS*, **486**, 3702
- Snyder, G. F., Torrey, P., Lotz, J. M., et al. 2015b, *MNRAS*, **454**, 1886
- Somerville, R. S., & Davé, R. 2015, *ARA&A*, **53**, 51
- Somerville, R. S., Popping, G., & Trager, S. C. 2015, arXiv:1503.0755
- Springel, V. 2010, *MNRAS*, **401**, 791
- Stark, D. P. 2016, *ARA&A*, **54**, 761
- Steidel, C. C., Gialvalisco, M., Pettini, M., Dickinson, M., & Adelberger, K. L. 1996, *ApJL*, **462**, L17
- Steinacker, J., Baes, M., & Gordon, K. D. 2013, *ARA&A*, **51**, 63
- Torrey, P., Snyder, G. F., Vogelsberger, M., et al. 2015, *MNRAS*, **447**, 2753
- Trayford, J. W., Camps, P., Theuns, T., et al. 2017, *MNRAS*, **470**, 771
- Trayford, J. W., Lagos, C. d. P., Robotham, A. S. G., & Obreschkow, D. 2020, *MNRAS*, **491**, 3937
- Tremmel, M., Karcher, M., Governato, F., et al. 2017, *MNRAS*, **470**, 1121
- Tuffs, R. J., Popescu, C. C., Völk, H. J., Kylafis, N. D., & Dopita, M. A. 2004, *A&A*, **419**, 821
- Turk, M. J., Smith, B. D., Oishi, J. S., et al. 2011, *ApJS*, **192**, 9
- van Dokkum, P. G., Franx, M., Kriek, M., et al. 2008, *ApJL*, **677**, L5
- Verstocken, S., Van De Putte, D., Camps, P., & Baes, M. 2017, *A&C*, **20**, 16
- Villaume, A., Conroy, C., & Johnson, B. D. 2015, *ApJ*, **806**, 82
- Vladilo, G. 1998, *ApJ*, **493**, 583
- Vogelsberger, M., Genel, S., Springel, V., et al. 2014, *MNRAS*, **444**, 1518
- Vogelsberger, M., Marinacci, F., Torrey, P., & Puchwein, E. 2020, *NatRP*, **2**, 42
- Wadsley, J. W., Stadel, J., & Quinn, T. 2004, *NewA*, **9**, 137
- Walcher, J., Groves, B., Budavári, T., & Dale, D. 2011, *Ap&SS*, **331**, 1
- Watson, D. 2011, *A&A*, **533**, A16
- Weingartner, J. C., & Draine, B. T. 2001, *ApJ*, **548**, 296
- Wetzel, A. R., Hopkins, P. F., Kim, J.-h., et al. 2016, *ApJL*, **827**, L23
- Younger, J. D., Hayward, C. C., Narayanan, D., et al. 2009, *MNRAS*, **396**, L66
- Zhang, H.-X., Puzia, T. H., & Weisz, D. R. 2017, *ApJS*, **233**, 13